Identification and experimental validation of ACSL1 as a critical ferroptosis-related gene in acute myocardial infarction

Ge Song *[a], Yuewen Qi *[b,c], Ying Zhang [a,b,d], Lingling Gao[a], Aoxue Mei[a], Enhong Xing[c], Linlin Wang [a], Yan Liu[a], Lixian Sun [a,b,d]

*contributed equally

[a]Department of Cardiology, The Affiliated Hospital of Chengde Medical University, Chengde, China;

[b]Hebei Key Laboratory of Panvascular Diseases, Chengde, China;

[c]Central Laboratory of Chengde Medical University Affiliated Hospital, Chengde, China

[d]The Cardiovascular Research Institute of Chengde, Chengde, China;

Correspondence: Lixian Sun

Department of Cardiology, The Affiliated Hospital of Chengde Medical University, Chengde, China

Hebei Key Laboratory of Panvascular Diseases, Chengde, China

The Cardiovascular Research Institute of Chengde, Chengde, China

No.36, Nanyingzi Street, Shuangqiao District, Chengde, Hebei Province, 067000, China

Tel: +86 0314 227 9016

Fax: +86 0314 227 4895

Email: lixiansun01@126.com

Abstract

Ischemic heart disease, particularly acute myocardial infarction (AMI), remains a primary cause of morbidity and mortality worldwide. The identification of new biomarkers is essential owing to the limited number of clinical indicators available for the early diagnosis of AMI. In this study, we analyzed FerrDB and GeneCards to identify ferroptosis-related genes (FRGs). Differentially expressed genes (DEGs) and co-expression modules were investigated by DEG analysis and weighted Gene Co-expression Network Analysis (WGCNA) using the Gene Expression Omnibus (GEO) database. Additionally, we employed unsupervised consensus clustering to classify AMI into subtypes, utilizing the Least Absolute Shrinkage and Selection Operator (LASSO) algorithm to effectively identify the most relevant characteristic genes. We selected the top three differentially expressed hub genes in the common intersection by integrating the performance of four machine learning techniques. A machine learning model for diagnosis was subsequently developed based on core genes, with its prediction accuracy validated using receiver operating characteristic (ROC) curves and two independent datasets. Additionally, LC-MS/MS and spatial transcriptomics were performed to verify the hub gene, acyl-CoA synthetase long-chain family member 1 (ACSL1). We validated ACSL1 expression in the HL-1 hypoxia cell model and AMI mice by RT-qPCR analysis. Western blotting and immunofluorescence experiments were conducted on mice after establishing the AMI model. Moreover, transfection and RT-qPCR were used to identify the effects of other ferroptosis-related genes in a cellular hypoxia model. Our findings reveal potential ferroptosis-related early AMI biomarkers and have significant implications for the early diagnosis of AMI.

Keywords: acyl-CoA synthetase long-chain family member 1 (ACSL1), ferroptosis, acute myocardial infarction, molecular cluster, proteomics, machine learning methods.

Background

Ischemic heart disease is the leading cause of death globally, and its prevalence continues to rise, with acute myocardial infarction (AMI) accounting for approximately 75% of all sudden cardiac deaths [1,2]. Myocardial ischemia and infarction are characterized by myocardial cell death resulting from prolonged ischemia [3]. AMI is generally triggered by the abrupt rupture of an atherosclerotic plaque, leading to thrombosis and subsequent acute ischemic hypoxic necrosis of the myocardium [4,5]. The pathological features comprise cardiomyocyte apoptosis, myocardial fibrosis, and myocardial remodeling, ultimately leading to heart failure and potentially fatal clinical outcomes, such as cardiogenic shock and death [6]. The primary objective in managing AMI is to restore blood flow to the heart as quickly as possible, minimizing the extent of myocardial damage [5]. However, despite thrombolytic and interventional treatments for AMI, mortality rates remain high [5,7]. Cardiac troponin I (cTnI) and cardiac troponin T (cTnT) are established AMI biomarkers. However, their levels may be elevated in other myocardial injuries, limiting their specificity in clinical settings [8]. Given the limited clinical indicators available for diagnosing and assessing the severity of AMI, it is crucial to explore new biomarkers for early diagnosis and severity evaluation.

The concept of 'ferroptosis' was first introduced in 2012. However, earlier instances of cell death resembling iron death were reported under the term 'oxidative death, ' referring to a form of cell death induced by oxidative stress [9]. Under healthy physiological conditions, there is a dynamic equilibrium between intracellular iron ion concentrations. An excessive accumulation of iron ions can result in membrane lipid peroxidation and subsequent oxidative stress, ultimately leading to cell death [10,11]. Previous studies have indicated that ferroptosis is a pathological event closely linked to inflammation [12] associated with conditions such as coronary artery disease and myocardial ischemia/reperfusion injury

[13–16]. Iron death is characterized by elevated levels of reactive oxygen species (ROS) and lipid peroxidation. Increased ROS levels significantly contribute to various cardiovascular disorders [15]. Lipid peroxidation and the accumulation of by-products can be attenuated through ferroptosis inhibition, thereby reducing cell death and alleviating myocardial ischemia-reperfusion injury [17–19]. The prevention of iron death and preservation of mitochondrial function may protect the heart from cardiomyopathy [20]. Nuclear factor erythroid-derived 2-related factor 2 (NRF2), an essential transcription factor, regulates ROS levels and maintains intracellular redox balance. Previous studies have demonstrated that the nuclear factor erythroid-derived 2-related factor 2/heme oxygenase-1 (NRF2/HO-1) pathway plays a protective role in cardiomyocytes against oxidative stress damage following myocardial infarction (MI), reducing cardiomyocyte apoptosis [21,22]. Furthermore, the primary iron storage proteins ferritin light chain/ferritin heavy chain (FTL/FTH1) and glutathione peroxidase 4 (GPX4) are regulated by NRF2. Targeting NRF2 presents a promising strategy for disease intervention aimed at modulating lipid peroxidation (LPO) and ferroptosis [23–27]. Therefore, ferroptosis-related genes hold the potential to serve as early diagnostic markers and therapeutic targets for AMI. However, their relationship requires further exploration.

This study aimed to identify ferroptosis-related genes (FRGs) as novel biomarkers for AMI diagnosis and treatment. We conducted a comprehensive analysis using the FerrDB and GeneCards databases to screen for FRGs, and investigated differentially expressed genes (DEGs) associated with AMI, as well as co-expression modules, using Weighted Gene Co-expression Network Analysis (WGCNA) from the Gene Expression Omnibus (GEO) database. Additionally, we employed unsupervised consensus clustering to classify AMI into subtypes, utilizing the Least Absolute Shrinkage and Selection Operator (LASSO) algorithm to effectively identify the most relevant characteristic genes. Four machine-learning models

were integrated to further screen and validate these genes, resulting in the identification of three hub genes (ACSL1, ZFP36, and CDKN1A) and the development of a machine-learning model for diagnosis. We established hypoxic HL-1 cells and an AMI mouse model. The core gene ACSL1 was verified through LC-MS/MS and spatial transcriptomics and validated in vitro and in vivo using RT-qPCR experiments. After establishing an AMI mouse model, western blot analysis and immunofluorescence assays were performed to validate the findings. Following the establishment of an HL-1 hypoxic cell model, transfections with ACSL1 and RT-qPCR were used to identify the effects of other ferroptosis-related genes. Simultaneously, WB experiments on HL-1 cells were performed to verify the transfection efficiency. Given the high mortality rate associated with AMI, early diagnosis and risk stratification are clinically crucial. This study provides significant insights into early AMI diagnosis, elucidates the role of hub genes in the ferroptosis pathway following AMI, and provides a theoretical foundation for identifying novel diagnostic methods and targeted therapies for AMI.

Methods

2.1. Establishment of ferroptosis-related genes（FRGs） signature

2.1.1. Data collection

Fig. 1 shows a basic flowchart of the study created using BioGDP.com [28]. We screened FRGs from the FerrDB and GeneCards databases. Additionally, the patients' relevant expression data were downloaded from the GSE66360 and GSE20681 datasets in the GEO online database (www.ncbi.nlm.nih.gov/geo) [29]. Information on the dataset is presented in **Table 1**.

2.1.2. WGCNA algorithm

The WGCNA algorithm was employed to identify cluster-specific and co-expressed modules in the GSE66360 dataset using the "WGCNA" package. The initial selection involved choosing the top quartile

of genes exhibiting the greatest variance, followed by the construction of a weighted adjacency matrix and topological overlap matrix (TOM) using the soft threshold power value in WGCNA. Module-trait associations were then evaluated by analyzing the correlation between clinical traits and signature genes, facilitating the identification of expression modules that strongly correlate with phenotypes [30,31].

2.1.3. Identification of DEFRGs and Functional Analysis

Differentially expressed genes (DEGs) between normal control and patients with AMI in GSE66360 were identified with the "Limma" package and visualized by the "heatmap", "ggplot2", and other R packages (p-value < 0.05). The significance criteria were established as an adjusted P-value <0.05 and |log2FC| > 1 for screening DEGs.

Differentially expressed ferroptosis-related genes (DEFRGs) were identified by examining FRGs, DEGs, and WGCNA in the GSE66360 dataset. The chromosomal mapping was conducted using the 'RCircos' package, a robust tool designed for visualizing genomic data and facilitating comprehensive analyses of chromosome structures. This methodological approach allows for effective representation and interpretation of genetic information, thereby enhancing the clarity and depth of the analysis. To further investigate the functional relevance of DEFRGs, we used Gene Ontology (GO) and Kyoto Encyclopedia of Genes and Genomes (KEGG) analyses, comprising various biological functions, including biological processes (BP), cellular components (CC), and molecular functions (MF). Additionally, a protein-protein interaction (PPI) network for DEFRGs was constructed using the STRING online database to analyze known and predicted protein interactions.

2.1.4. Immune characteristic analysis

The CIBERSORT algorithm and LM22 feature matrix were used to estimate the relative abundance of 22 immune cell types based on gene expression data. CIBERSORT operates as a deconvolution

algorithm, allowing the transformation of a normalized gene expression matrix into a detailed composition of infiltrating immune cells [32]. The proportions of each immune cell type within individual samples sum to one, ensuring a comprehensive representation of the immune profile. To investigate the relationships between various genes, we utilized the "circlize" and "corrplot" R packages, which facilitate data visualization and analysis. Namely, Spearman's correlation analysis was applied to assess the correlation between gene expression levels and immune cell infiltration percentage, with a P-value of less than 0.05 indicating a significant correlation. We additionally employed the "corrplot" R package to effectively visualize our findings.

2.1.5. Unsupervised clustering for patients with AMI

We conducted an unsupervised cluster analysis on the expression profiles of DEFRGs using the "ConsensusClusterPlus" R package, aiming to effectively classify the data into two distinct clusters by applying the k-means algorithm. To determine the optimal number of clusters, we conducted a thorough assessment that included several evaluation metrics, such as the consistent clustering score, which was required to exceed 0.8, cumulative distribution function (CDF) curves, and consensus matrices. Our evaluation indicated that the maximum number of identified subtypes, denoted by k, was six.

2.1.6. Principal component analysis (PCA)

PCA was conducted randomly between the two identified clusters to ensure that no interference affected the dimensionality reduction process. This approach is recognized as an effective technique for reducing the dimensionality of datasets. In our study, the variables were linearly aligned to elucidate the most significant differences between Clusters 1 and 2. This coordination of variables was accomplished with a focus on data decentralization, which played a crucial role in enhancing the clarity of the distinctions between the two clusters.

2.1.7. Identification of hub genes by machine learning models

We applied the LASSO algorithm to effectively identify the most relevant characteristic genes. This analysis was performed using the R package "glmnet" with 10-fold cross-validation for data dimensionality reduction and variable selection [33]. We then intersected the DEGs, FRGs, Cluster-related genes, and WGCNA GREEN results with the LASSO analysis to identify cross-talk genes using the "Venn" package.

To ensure thorough validation and screening of the hub genes identified in this study, a comprehensive approach was adopted by constructing four distinct machine learning models. These include Xtreme Gradient Boosting (XGB), the generalized linear model (GLM), the random forest model (RF), and the support vector machine model (SVM). The implementation of these models was facilitated through the "caret" R package, designed for streamlining the model training process in R. The XGB model uses an eXtreme Gradient Boosting algorithm employing the XGBoost package. This algorithm is recognized for its ability to gradually create a base model that can optimally approximate the objective function, thereby improving predictive performance [34]. In contrast, GLM represents an advancement of the traditional linear regression approach, enabling the analysis of response variables that are not normally distributed [35] by providing a direct and succinct linear transformation of models that may be inherently nonlinear. SVM, another pivotal model utilized in this analysis, is a widely researched machine-learning method, particularly used for addressing both classification and regression tasks [36]. Furthermore, the RF model is recognized as a leading machine-learning technique characterized by its nonparametric nature, allowing it to handle various types of response variables, including categorical and quantitative outcomes as well as time-to-event data [37]. Furthermore, the RF model mechanism involves training base learners on random subsets of data and aggregating their predictions to deliver a robust final output from an

ensemble. The analysis benefited from the capabilities of the "DALEX" and "caret" R packages, which facilitated the establishment of the mentioned machine learning models. All the parameters within these models were automatically adjusted to optimize their performance.

Additionally, visualizations of the residual distribution and feature importance are provided, enabling deeper insights into the functioning of the model. The area under the Receiver Operating Characteristic (ROC) curve was assessed using the "pROC" package, further enhancing model performance evaluation. Through this rigorous modeling process, the top three genes displaying consistent interactions across the models were selected as hub genes relevant to AMI.

2.1.8. Prediction model Construction and External dataset validation

A nomogram model was developed utilizing three predictive genes, employing the "rms" R package, to evaluate the likelihood of AMI occurring. In this model, each predictive variable is assigned a corresponding point value, allowing for a more systematic assessment of the risk factors. The "total points" in the nomogram are calculated by summing the individual points assigned to each of the three predictive genes, providing a cumulative score that reflects the overall risk assessment for AMI.

The GSE20681 dataset, consisting of independent whole blood samples, includes a cohort of 99 patients diagnosed with AMI and an equal number of normal controls. The dataset was obtained from the online GEO database. The findings derived from this dataset served as external validation of the predictive efficacy of the established model. To enhance understanding and interpretation of the results, the data were subsequently visualized using the "pROC" R package, which facilitates the graphical representation of ROC curves.

2.1.9 Processing of spatial transcriptome sequencing

Spatial transcriptome sequencing data analysis was used to associate gene expression information

with the spatial position of the tissues. Following coordinate positioning and capture area calibration on tissue sections, a gene expression matrix containing spatial location information was generated. The 'Seurat' package was used to construct spatial-specific objects (through the Create Spatial Seurat Object function), and the 'Harmony' package was employed for batch effect correction. This algorithm effectively eliminates technical variations between different samples by aligning cell distributions in a shared latent space. Moreover, through spatial clustering analysis, combined with gene expression profiles and spatial proximity relationships, cell subpopulations with similar expression patterns and spatial locations were identified using a graph-clustering algorithm. For visualization, the 'SpatialFeaturePlot' function (a built-in feature of Seurat) was used to intuitively present the spatial distribution patterns of specific genes on tissue sections. Additionally, a trend analysis algorithm was used to identify genes enriched in specific anatomical regions in order to explore spatial heterogeneity. Biological validation was performed in combination with histological morphology to achieve accurate mapping of gene expression patterns and tissue structures.

2.2. Hub gene validation and analysis

2.2.1. Cell Culture and Transfection

HL-1 cells were obtained from Sios Biotechnology Co., Ltd. (Wuhan, China). HL-1 cardiomyocytes were cultured in MEM + 10% FBS + 1% penicillin–streptomycin solution. A previous study was used to construct the hypoxia model. HL-1 cardiomyocytes were cultured for 12 h in an anaerobic glove box containing 5% CO2, 1% O2, and 94% N2 [38,39].

The siRNAs, pcDNA, and a negative control (NC) were procured from Weihuan Biotechnology Co., Ltd. (Shanghai, China). HL-1 cells were plated in 6-well plates at a density of 1 × 10^5 cells per well and allowed to grow until they reached 30–50% confluence, which was optimal for transfection. Transfection

was carried out using Lipofectamine 3000 (GIBCO, China) at a final concentration of 50 μM. After 48 h, the effects of siRNA transfection or overexpression were assessed using qRT-PCR and western blotting. Successfully transfected cells were used for subsequent experiments.

2.2.2. Acute myocardial infarction model created

Male C57BL/6 mice (6–8 weeks old) were obtained from Chongqing Xinyue Biotechnology Co., LTD (Chongqing, China) and randomly assigned to either the AMI or sham group. The process was conducted using a random number table. Mice were housed in a temperature-controlled environment with 12 h light/12 h dark cycles and allowed to acclimate for 1 week before surgery. Subsequently, the left pectoralis major and pectoralis minor muscles were separated, under isoflurane anesthesia, to access the heart, and the left anterior descending (LAD) coronary artery was ligated to trigger regional ischemia. In the sham surgery, the same procedure was performed, except for the LAD ligation. Twenty-four hours after myocardial infarction, echocardiography was conducted to assess alterations in the left ventricular ejection fraction (LVEF) and fractional shortening (LVFS) [40,41]. After euthanasia, cardiac tissue and peripheral blood samples were collected. The animal study protocol was approved by the Animal Care and Use Committee of the Affiliated Hospital of Chengde Medical University. This study was approved by the Ethics Committee of the Affiliated Hospital of Chengde Medical University (approval number: CYFYLL2024600).

2.2.3. TTC staining

Hearts from mice in different groups were frozen at a −20°C refrigerator for 20-30 min, then sequentially cut into 0.1 cm thick slices from top to bottom. The slices were then incubated at 37°C with a prepared TTC solution for 25-35 min, fixed in 4% polyformaldehyde solution for 4-24 hours, and photographed with a digital camera from biggest to smallest, allowing for the continuous observation and

distinction of infarction sizes in the myocardium [42].

2.2.4. RNA isolation and Real-Time quantitative PCR (RT-qPCR) analysis

Total RNA was extracted from HL-1 cells or cardiac tissues using the TRIzol reagent. cDNA was synthesized and amplified using the FastKing cDNA First Chain Synthesis Kit (KR116, TIANGEN), according to the manufacturer's instructions. cDNA was amplified by RT-qPCR using SuperReal PreMix Plus (SYBR Green) (FP205, TIANGEN). The reaction conditions were set as follows: 95 ◦C, 10 s; 50-60 ◦C, 20 s; 72 ◦C, 20-32 s for 40 cycles. Data analysis was performed using $2^{-\Delta\Delta Ct}$ to express the relative changes in gene expression. GAPDH was used as the internal control. The RT-qPCR primer sequences are listed in **Table 3**.

2.2.5. Western blotting analysis

The concentration of proteins extracted from the tissues was determined using the BCA protein assay kit (SK1070, COOLABER SCIENCE & TECHNOLOGY Co., LTD). The proteins in each group were then separated by 12% sodium dodecyl sulfate (SDS)-polyacrylamide gel electrophoresis (PAGE) and transferred to polyvinylidene difluoride membranes (PVDF, 0.45 μm, MerckMillipore). Subsequently, the Protein Free Rapid Blocking Buffer (5×) (PS108, Shanghai Yase Biomedical Technology Co., LTD) was used to block the nonspecific antigens in the membranes for 10 minutes, followed by a 4 °C overnight incubation of the membranes with the primary antibodies [including antibodies against ACSL1 (1:4000, Proteintech Group), GPX4 (1:5000, Abcam) and GAPDH (1:2500, Abcam)]. Membranes were incubated with anti-rabbit IgG (BF03008, Biodragon) as the secondary antibody for 1 h at room temperature. After using an enhanced chemiluminescence (ECL) substrate, the blots were analyzed using a chemiluminescence detection system (C300).

2.2.6. Immunohistochemical (IHC) staining

Paraffin-embedded heart sections were deparaffinized and rehydrated using an ethanol gradient, and antigen retrieval was performed using a sodium citrate buffer according to the primary antibody. The sections were then processed according to the instructions of the UltraSensitive SP (rabbit) IHC kit (KIT-9706-6 ml, MXB Biotechnologies) and DAB kit (ZLI-9018, ZSGB-BIO). The primary antibodies used for IHC targeted ACSL1 (1:150; Proteintech Group) and GPX4 (1:150; Abcam). Finally, the images were captured using a digital microscope (BX60-32FB3-E01).

2.2.7. Proteomics

LC-MS/MS was performed using TIANGEN (Wuhan, China). Tissue samples were collected from the infarcted areas of the heart and from the control group. The protein was digested with a protease to obtain peptides. The separated peptides were then analyzed using a Q Exactive HF (X) mass spectrometer (Thermo Fisher Scientific). The software PD 2.2 further filtered the mass spectrum data. Subsequently, the protein quantification results were statistically analyzed using a t-test, with proteins whose levels were significantly different between the experimental and control groups ($p < 0.05$, $|\log2FC| > 1$) defined as differentially expressed proteins (DEP).

2.3. Statistical analysis

Statistical analyses were conducted using R software (version 4.3.1), GraphPad Prism (Version 8.0.2), and SPSS (Version 26.0). The normality of the distribution of continuous variables was confirmed using the Kolmogorov–Smirnov test. Normally distributed variables were presented as the mean±standard deviation, and non-normally distributed variables as the median with interquartile range. Student's t-test and Mann–Whitney U test were used to test continuous variables with or without a normal distribution, respectively. Categorical variables were presented as numbers (percentages) using the chi-square test. Bartlett's test was used to evaluate the homogeneity of variance. Spearman's correlation analysis was used

to identify the correlations. Statistical significance was set at $P < 0.05$ (two-sided).

Results

3.1. Identification of DEFRGs and Variations of immune characteristics in AMI samples

Twenty-five differentially expressed genes associated with ferroptosis (DEFRGs) were identified through the intersection of DEGs, FRGs, and WGCNA in the GSE66360 dataset (**Fig. 2 A-F**). To clarify the role of DEFRGs in AMI progression, we first characterized the expression of 25 DEFRGs in AMI samples and normal controls using the GSE66360 dataset, and screened 17 DEFRGs (**Fig. 3A-C**, including ACSL1, ZFP36, CDKN1A, TLR4, PDK4, G0S2, SPI1, DDIT3, HP, DUSP1, IL1B, NCF2, CXCL2, TNF, PGD, RPL36A, and LCN2. We then conducted a correlation analysis of the DEFRGs to assess the interactions between these genes within the context of AMI. The resulting relationship network illustrated a strong interplay among the DEFRGs, as shown in **Fig. 3D and E**. Notably, we found that ACSL1 was positively correlated with TLR4 and SPI1.

Employing the CIBERSORT algorithm, we conducted an immune infiltration analysis to evaluate the differences in the proportions of 22 types of immune-infiltrating cells between AMI samples and normal controls. The findings revealed an increased prevalence of several immune cell types, including activated memory CD4+ T cells, follicular helper T cells, activated natural killer (NK) cells, monocytes, activated mast cells, and neutrophils within AMI samples, as shown in **Fig. 3F**, suggesting that the inflammatory response plays a significant role in the pathogenesis of AMI. To further investigate the role of these identified genes in the inflammatory response specific to patients with AMI, we conducted a correlation analysis to explore the relationships between DEFRGs and various immune-infiltrating cells. Our analysis revealed that neutrophils correlated with all DEFRGs presented in **Fig. 3G**. Among these relationships,

ACSL1 exhibited the most notable negative correlation with resting memory CD4+ T cells and a positive correlation with neutrophils. Additionally, ACSL1 and IL1B demonstrated a significant positive correlation with activated mast cells ($p < 0.001$). Through this comprehensive analysis, it is evident that DEFRGs may have a substantial impact on the immune response in individuals with AMI.

Subsequently, we conducted GO and KEGG analyses to elucidate potential characteristics. These DEFRGs were significantly enriched in processes related to atherosclerosis, such as cellular responses to biotic stimuli, specific granule lumen, cytokine receptor binding, and lipid metabolism (**Fig. 4A**). A PPI network was created, comprising 23 DEFRGs organized into a composite of cogenes (**Fig. 4B**).

3.2. Characterization of ferroptosis-related clusters and variations of immune characteristics

AMI samples were clustered based on the expression profiles of these DEFRGs using a consensus clustering algorithm. The optimal number of clusters was two, as supported by the stabilization of clustering outcomes (**Fig. 5A**). As the value of k varied from 2 to 6, variations in the cumulative distribution function (CDF) curves for k-1 and k were represented by the area under the curve (**Fig. 5B**). The CDF curves exhibited fluctuations across a narrow consensus index range, particularly between 0.3 and 0.6 (**Fig. 5C**). Notably, the concordance score for each subtype exceeded 0.8 only at $k = 2$ (**Fig. 5D**). Consequently, the samples were categorized into two distinct subtypes, termed Cluster 1 and Cluster 2, followed by a principal component analysis (PCA), whose results demonstrated a significant difference between Clusters 1 and 2 in terms of the expression levels of DEFRGs (**Fig. 5E**).

Variations in DEFRGs expression between Clusters 1 and 2 were analyzed to investigate the molecular signatures. The results indicated that cluster 1 exhibited higher levels of all genes (**Fig. 6A and B**). Furthermore, Cluster 1 demonstrated elevated ratios of monocytes, activated mast cells, and

neutrophils, whereas Cluster 2 displayed a greater proportion of memory B cells, plasma cells, CD8+ T cells, naïve CD4+ T cells, resting memory CD4+ T cells, activated memory CD4+ T cells, and gamma-delta T cells (**Fig. 6C and D**).

3.3. Identification of hub genes for diagnosing AMI

Unsupervised consensus clustering was used to classify the AMI into subtypes. Ferroptosis phenotype clusters were analyzed using the WGCNA package tool. Co-expression modules were identified using a soft power value of 12 and a scale-free $R^2 = 0.9$ (**Fig. 7A**). We identified six distinct gene coexpression modules using a dynamic cutting algorithm (**Fig.7B**). Correlation analysis suggested a close association between ferroptosis-related clusters and the green module (**Fig. 7C**). Finally, we constructed a scatterplot of Gene Significance versus Module Membership in the green module (**Fig. 7D**). To further streamline the important characteristic variables, we performed LASSO analysis, identifying 13 genes in AMI (**Fig 7E, F**). By intersecting the WGCNA GREEN, GSE66360 DEGs, Cluster WGCNA, LASSO analysis, and FRGs, we identified 11 crosstalk genes (**Fig. 8A**).

Subsequently, four machine learning models (SVM, RF, GLM, and XGB) were built based on the expression signatures of the 11 cross-talk genes to further explore genes with relatively higher predictive values. The five most important variables of each model were displayed based on the root mean square error (RMSE) loss after permutations (**Fig. 8B-E**). Through the four machine learning methods, we selected the top three differentially expressed genes (ACSL1, ZFP36, and CDKN1A), which were in common intersection, as hub genes (**Fig. 8F**).

3.4. Establishment and validation of the prognostic prediction model

A nomogram was constructed based on the GSE66360 dataset (**Fig. 9A**). The receiver operating characteristic (ROC) curve demonstrated strong discriminatory power with an area under the curve (AUC)

of 0.958 (95% confidence interval [CI]: 0.922–0.994) in the GSE66360 dataset for evaluating the diagnostic performance of the 3-gene signature model (**Fig. 9B**). Fig. 10 presents the ROC curve analyses used to determine the optimal cutoff values for the three most important variables (ACSL1, ZFP36, and CDKN1A) in the GSE66360 dataset. The AUC for ACSL1 was 0.872 (95% CI: 0.798–0.938) (**Fig.9E**), 0.854 (95% CI: 0.774–0.922) for ZFP36 (**Fig. 9F**), and 0.881 (95% CI: 0.798–0.947) for CDKN1A (**Fig.9G**).

An external dataset (GSE20681) was used to validate the predictive model (**Fig. 9C**), revealing discriminatory ability with an AUC of 0.626 (95% CI: 0.549–0.703) in the GSE20681 dataset for validating the diagnostic model's performance. (**Fig. 9D**).

3.5. Identification and Validation of the hub gene

Following surgical procedures on the mice, a cardiac ultrasound was used to assess alterations in cardiac function. Compared to the sham group, the left ventricular internal diameter of mice in the AMI group exhibited significant increases during both diastole and systole ($P < 0.001$) **(Fig. 10A, B; Table 4)**. Additionally, both ejection fraction and fractional shortening were significantly reduced ($P < 0.001$), indicating impaired cardiac function. The results of the TTC staining are illustrated in **Fig. 10C and D**, where no white infarct areas were observed in the sham group. In contrast, the AMI group exhibited distinct pale infarct regions and an enlarged cardiac cavity, indicating myocardial infarction. The ECG results also showed significant differences between the AMI and sham groups, confirming the successful establishment of the model (**Fig. 10E, F**).

Following label-free quantitative proteomic analysis, 2,345 quantifiable proteins were obtained. Based on the screening criteria, 599 differentially expressed proteins were identified, among which ACSL1 was significantly downregulated in the AMI group compared to the sham group **(Fig. 11A)**.

Spatial transcriptomics is a gene expression analysis technique that preserves the spatial structure information of tissues. Its core value lies in overcoming the limitations of traditional single-cell sequencing, which loses the spatial position information of cells, and can directly correlate gene expression patterns with the anatomical structure and cellular microenvironment of the tissue. Spatial transcriptomic analysis of two AMI mouse samples and two sham samples based on cell type classification revealed a clear separation between cells of different colors in the AMI and sham groups. Additionally, distinct gene expression characteristics were observed within the AMI tissue across the infarction, junction, and normal areas. Changes in the expression of the hub gene ACSL1 were directly located in specific pathological regions. The spatial plot displays an X-axis and Y-axis corresponding to the real physical coordinates of tissue sections, with each point (spot) representing a region captured by sequencing based on the resolution of the sequencing platform, and the color of the spots reflecting the molecular characteristics. Spatial plots show spatial maps of the predicted ACSL1 scores in the AMI lesion area (identified by H&E staining, GEO database, sample IDs: GSM 6613087, GSM 6613088, GSM 6613080, and GSM 6613081). Through H&E staining, the tissue structure (such as the myocardial cell layer, blood vessels, stroma, core infarction area (nucleus-free necrotic area), junction area (surviving but stressed tissue around the infarction), and distal normal area were identified. ACSL1 expression was high in the normal myocardial layer, absent in the AMI infarction area, and upregulated in the junction area (metabolic adjustment during stress). (**Fig.11B**).

To further investigate the mRNA and protein expression levels of the hub genes in vivo and in vitro, we constructed an HL-1 hypoxia model, an AMI mouse model, and blood samples from patients with AMI. qRT-PCR was used to verify the mRNA levels of the three hub genes in both in vitro cell models and in vivo tissues. As shown in **Fig. 12**, ACSL1 displayed significantly lower expression levels in both

cells and tissues in the model group than in the control group.

Additionally, western blotting revealed significant protein changes in the cardiac muscle tissues of mice. ACSL1 and GPX4, key ferroptosis-related genes, were significantly downregulated in the hearts of mice with AMI compared to those in the sham group in **Fig.12A, Band C**. The results of IHC staining were similar (**Fig. 12D-G**).

To further elucidate the biological function of ACSL1 in HL-1 cells, we silenced and overexpressed ACSL1 in an HL-1 hypoxic model using siRNA and plasmids. The effects of silencing and overexpression by RT-qPCR were then verified, as shown in **Fig. 13**. ACSL1 mRNA expression in HL-1 cells was significantly downregulated after siRNA-ACSL1 transfection and upregulated after pcDNA-ACSL1 transfection, as shown in **Fig. 13**. Additionally, the effects of an altered expression of ACSL1 in HL-1 cells on key indicators such as NRF2, HO-1, SLC7A11, and SLC40A1 were examined. The results demonstrated that, along with the changes in ACSL1, the expression of NRF2, HO-1, SLC7A11, and SLC40A1 in the HL-1 hypoxic cell model was significantly altered compared to the NC group (**Fig. 13**), suggesting that ACSL1 plays a vital role in blocking ferroptosis in HL-1 cells. These trends were additionally confirmed to be consistent at the protein level **(Fig. 14)**.

Discussion

AMI is the predominant cause of mortality in individuals with cardiovascular disease. Despite advancements in thrombolytic and interventional treatments that have enhanced prognosis, mortality rates continue to be significantly elevated [5]. Identifying effective diagnostic biomarkers for the early prediction of AMI is crucial for improving therapeutic efficiency and patient outcomes. Recently, ferroptosis has become a popular research topic. Ferroptosis is a form of regulated cell death characterized by iron-dependent lipid peroxidation. Accumulating evidence has demonstrated that ferroptosis is a critical

player in AMI pathogenesis [13,14,43–45]. However, the mechanism underlying ferroptosis in the pathological process of AMI remains unclear and requires further investigation.

In our study of the mechanism of AMI, we used ACSL1 as the main research factor. ACSL1 is a pivotal enzyme that catalyzes the conversion of fatty acids into acyl-CoA esters, which are essential for lipid biosynthesis and remodeling. A growing number of studies suggest that ACSL1 promotes the incorporation of polyunsaturated fatty acids (PUFAs) into phospholipids, causing cells to be more susceptible to lipid peroxidation and enhancing cell resistance to ferroptosis [46–49]. In addition, deletion of ACSL1 in myeloid cells inhibited the inflammatory effect of diabetes mellitus on monocytes and macrophages and protected mice against lesions of diabetes-induced atherosclerosis in a T1DM mouse model [50]. In an AMI study, the expression of ACSL1 in peripheral blood may be a molecular marker for assessing the risk of AMI [51]. In a previous study, ACSL1 expression was also significantly correlated with immune cell infiltration [52,53]. However, studies on the mechanisms underlying ACSL1 function are currently limited. In our immune infiltration analysis, Cluster 1 showed elevated ratios of monocytes, activated mast cells, and neutrophils. ACSL1 showed the strongest positive correlation with neutrophils and activated mast cells. During an AMI, the immune response is activated, resulting in a significant infiltration of neutrophils and activated mast cells into the infarcted area. This change in infiltration suggests that the inflammatory response plays a crucial role in AMI pathogenesis because the aggregation of numerous immune cells represents the body's immune response to myocardial injury. In our in vivo and in vitro experimental studies, ACSL1 was confirmed to have a specific differential expression in AMI. ACSL1 may play a pivotal role in the immune response of patients with AMI by influencing the function of neutrophils and activated mast cells, indicating a complex regulatory relationship between them.

However, the specific regulatory role of ACSL1 in AMI immune cell infiltration requires further investigation.

In this study, we examined the expression of other ferroptosis-related factors, such as GPX4, HO-1, NRF2, SLC7A11, and SLC40A1, in vivo and in vitro, and whether their regulation is affected by ACSL1. GPX4 is the core molecular gate of ferroptosis and is regarded as the final regulatory node of the ferroptosis pathway. GPX4 inactivation is necessary for ferroptosis [17,54]. Therefore, we used GPX4 as a marker to prove the occurrence of ferroptosis. Western blotting and pathological experiments showed that GPX4 levels were consistently decreased in the model group. Previous studies have demonstrated that NRF2 plays a crucial role in combating oxidative stress responses and heart remodeling after MI. Deletion of NRF2 induced significantly higher mortality in mice after MI than in mice in the control group. HO-1, regulated by the transcription factor NRF2, is a key antioxidant enzyme that degrades heme into biliverdin, carbon monoxide, and free iron [10,24]. While HO-1 exerts cytoprotective effects by reducing oxidative stress, it releases free iron, which can exacerbate ferroptosis [10,23]. The NRF2/HO-1 pathway plays a complex role in ferroptosis. We further revealed the role of ACSL1 in the interplay of the AMI ferroptosis pathway. siRNA or plasmid transfection and qRT-PCR were used to identify the effects of the NRF2/HO-1 pathway on the HL-1 hypoxic cell model. The mRNA results showed that the expression levels of NRF2 and HO-1 were significantly lower after silencing ACSL1 in HL-1 cells under hypoxic conditions, whereas higher expression was observed when ACSL1 was overexpressed. These findings highlight the potential of targeting ACSL1 to mitigate ferroptosis and improve cardiac outcomes. Targeting ACSL1 to regulate the NRF2/HO-1 pathway is a promising strategy for the treatment of AMI. A previous study demonstrated that NRF2 deficiency results in the downregulation of SLC7A11 expression and increased sensitivity to ferroptosis, confirming the importance of the NRF2-SLC7A11 axis in maintaining redox homeostasis [55].

NRF2 regulates iron metabolism and oxidative stress by controlling SLC7A11 (cystine uptake) and SLC40A1 (iron export) [56]. In our study, the expression of SLC7A11 and SLC40A1 was subject to ACSL1 regulation; however, whether they are directly regulated by ACSL1 or related to the function of NRF2 remains to be verified.

Conclusion

ACSL1, a novel ferroptosis-related biomarker and hub gene for early AMI diagnosis, regulates ferroptosis pathways in AMI. These findings establish a method to tailor diagnostic and therapeutic strategies using ACSL1 as a promising candidate biomarker. Future studies on core gene-specific regulatory networks and clinical translational values are warranted to advance AMI management.

List of abbreviations

ACSL1: Acyl-CoA Synthetase Long Chain Family Member 1

AMI: Acute Myocardial Infarction

AUC: Area Under the Curve

CDF: Cumulative Distribution Function

CI: Confidence Interval

cTnI: Cardiac Troponin I

cTnT: Cardiac Troponin T

DEGs: Differentially Expressed Genes

DEFRGs: Differentially Expressed Ferroptosis-Related Genes

DEP: Differentially Expressed Proteins

ECG: Electrocardiogram

FRGs: Ferroptosis-Related Genes

FTH1: Ferritin Heavy Chain 1

FTL: Ferritin Light Chain

GEO: Gene Expression Omnibus

GLM: Generalized Linear Model

GO: Gene Ontology

GPX4: Glutathione Peroxidase 4

HO-1: Heme Oxygenase-1

IHC: Immunohistochemistry

KEGG: Kyoto Encyclopedia of Genes and Genomes

LAD: Left Anterior Descending

LASSO: Least Absolute Shrinkage and Selection Operator

LC-MS/MS: Liquid Chromatography with Tandem Mass Spectrometry

LPO: Lipid Peroxidation

LVEF: Left Ventricular Ejection Fraction

LVFS: Left Ventricular Fractional Shortening

MI: Myocardial Infarction

NRF2: Nuclear Factor Erythroid 2–Related Factor 2

PCA: Principal Component Analysis

PPI: Protein-Protein Interaction

RF: Random Forest

RMSE: Root Mean Square Error

ROC: Receiver Operating Characteristic

ROS: Reactive Oxygen Species

RT-qPCR: Quantitative Reverse Transcription Polymerase Chain Reaction

SVM: Support Vector Machine

TOM: Topological Overlap Matrix

TTC: Triphenyltetrazolium Chloride

WGCNA: Weighted Gene Co-expression Network Analysis

XGB: eXtreme Gradient Boosting

Declarations

Ethics approval and consent to participate

The animal study protocol was approved by the Animal Care and Use Committee of the Affiliated Hospital of Chengde Medical University. This study was approved by the Ethics Committee of the Affiliated Hospital of Chengde Medical University (approval number: CYFYLL2024600).

Consent for publication

Not Applicable.

Availability of data and materials

The raw data supporting the conclusions of this article are available from the authors whenever needed. To obtain access to the raw data analyzed in this study, please contact Lixian Sun with email. Datasets supporting the conclusions of this study are available in the GEO database (https://www. ncbi. nlm. nih. gov/geo/).

Competing interests

The authors report no conflicts of interest in this work.

Funding

This study was supported by the Natural Science Foundation of Hebei Province (grant number H2025406001) awarded to Dr. Lixian Sun.

Authors' contribution

GS contributed to writing the original draft, visualization, formal analysis, software and conceptualization. YQ contributed to writing the original draft, visualization, methodology and data curation. YZ contributed to writing-review and editing, resources and data curation. LG contributed to resources, visualization and formal analysis. AM contributed to methodology and data curation. EX contributed to methodology and conceptualization. LW contributed to formal analysis and conceptualization. YL contributed to software and conceptualization. LS contributed to writing-review and editing, funding acquisition, and supervision.

Acknowledgements

The authors thank the doctors and nurses of the Cardiology Research Team and Laboratory Research Team at the Affiliated Hospital of Chengde Medical University and Hebei Key Laboratory of Panvascular Diseases for their assistance.

Authors' information

Ge Song, gesong0809@163.com

Yuewen Qi, qiyuewen900@126.com

Ying Zhang, cyfyzy@126.com

Lingling Gao, gaolingling0932@163.com

Aoxue Mei, meiaoxuemail@163.com

Enhong Xing, xeh001@sina.com

Linlin Wang, wanglinlincyfy@126.com

Yan Liu, 18822159543@163.com

Lixian Sun, lixiansun01@126.com

Reference

[1] B. Ibanez, S. James, S. Agewall, M.J. Antunes, C. Bucciarelli-Ducci, H. Bueno, A.L.P. Caforio, F. Crea, J.A. Goudevenos, S. Halvorsen, G. Hindricks, A. Kastrati, M.J. Lenzen, E. Prescott, M. Roffi, M. Valgimigli, C. Varenhorst, P. Vranckx, P. Widimský, ESC Scientific Document Group, ESC Guidelines for the management of acute myocardial infarction in patients presenting with ST-segment elevation, Eur. Heart J. 39 (2018) 119–177. doi.org/10.1093/eurheartj/ehx393.

[2] G.W. Reed, J.E. Rossi, C.P. Cannon, Acute myocardial infarction, Lancet. 389 (2017) 197–210. doi.org/10.1016/S0140-6736(16)30677-8.

[3] K. Thygesen, J.S. Alpert, A.S. Jaffe, B.R. Chaitman, J.J. Bax, D.A. Morrow, H.D. White, Executive Group on behalf of the Joint European Society of Cardiology (ESC)/American College of Cardiology (ACC)/American Heart Association (AHA)/World Heart Federation (WHF) Task Force for the Universal Definition of Myocardial Infarction, Fourth universal definition of myocardial infarction (2018), J. Am. Coll. Cardiol. 72 (2018) 2231–2264. doi.org/10.1016/j.jacc.2018.08.1038.

[4] L. Scheldeman, P. Sinnaeve, G.W. Albers, R. Lemmens, F. Van De Werf, Acute myocardial infarction and ischaemic stroke: Differences and similarities in reperfusion therapies—A review, Eur. Heart J. 45 (2024) 2735–2747. doi.org/10.1093/eurheartj/ehae371.

[5] F.G.P. Welt, W. Batchelor, J.R. Spears, C. Penna, P. Pagliaro, B. Ibanez, S.G. Drakos, G. Dangas, N.K. Kapur, Reperfusion injury in patients with acute myocardial infarction: JACC scientific statement, J. Am. Coll. Cardiol. 83 (2024) 2196–2213. doi.org/10.1016/j.jacc.2024.02.056.

[6] M. Gulati, P.D. Levy, D. Mukherjee, E. Amsterdam, D.L. Bhatt, K.K. Birtcher, R. Blankstein, J. Boyd,

R.P. Bullock-Palmer, T. Conejo, D.B. Diercks, F. Gentile, J.P. Greenwood, E.P. Hess, S.M. Hollenberg, W.A. Jaber, H. Jneid, J.A. Joglar, D.A. Morrow, R.E. O'Connor, M.A. Ross, L.J. Shaw, 2021 AHA/ACC/ASE/CHEST/SAEM/SCCT/SCMR guideline for the evaluation and diagnosis of chest pain: A report of the American College of Cardiology/American Heart Association joint committee on clinical practice guidelines, Circulation. 144 (2021) e368–e454. doi.org/10.1161/CIR.0000000000001029.

[7] M. Galli, G. Niccoli, G. De Maria, S. Brugaletta, R.A. Montone, R. Vergallo, S. Benenati, G. Magnani, D. D'Amario, I. Porto, F. Burzotta, A. Abbate, D.J. Angiolillo, F. Crea, Coronary microvascular obstruction and dysfunction in patients with acute myocardial infarction, Nat. Rev. Cardiol. 21 (2024) 283–298. doi.org/10.1038/s41569-023-00953-4.

[8] I.A. Katrukha, A.G. Katrukha, Myocardial injury and the release of troponins I and T in the blood of patients, Clin. Chem. 67 (2021) 124–130. doi.org/10.1093/clinchem/hvaa281.

[9] B.S.P. Shirlee Tan, B.S.P. David Schubert, B.S.P. Pamela Maher, Oxytosis: A novel form of programmed cell death. *CTMC*, Curr. Top. Med. Chem. 1 (2001) 497–506. doi.org/10.2174/1568026013394741.

[10] X. Jiang, B.R. Stockwell, M. Conrad, Ferroptosis: Mechanisms, biology and role in disease, Nat. Rev. Mol. Cell Biol. 22 (2021) 266–282. doi.org/10.1038/s41580-020-00324-8.

[11] S.W. Ng, S.G. Norwitz, E.R. Norwitz, The impact of iron overload and ferroptosis on reproductive disorders in humans: Implications for preeclampsia, Int. J. Mol. Sci. 20 (2019) 3283. doi.org/10.3390/ijms20133283.

[12] Q. Xiang, X. Yi, X.H. Zhu, X. Wei, D.S. Jiang, Regulated cell death in myocardial ischemia–reperfusion injury, Trends Endocrinol. Metab. 35 (2024) 219–234. doi.org/10.1016/j.tem.2023.10.010.

[13] J. Fan, T. Zhu, X. Tian, S. Liu, S.L. Zhang, Exploration of ferroptosis and necroptosis-related genes

and potential molecular mechanisms in psoriasis and atherosclerosis, Front. Immunol. 15 (2024) 1372303. doi.org/10.3389/fimmu.2024.1372303.

[14] Z. Song, J. Wang, L. Zhang, Ferroptosis: A new mechanism in diabetic cardiomyopathy, Int. J. Med. Sci. 21 (2024) 612–622. doi.org/10.7150/ijms.88476.

[15] Y. Wang, J. Wu, Ferroptosis: A new strategy for cardiovascular disease, Front. Cardiovasc. Med. 10 (2023) 1241282. doi.org/10.3389/fcvm.2023.1241282.

[16] C. Liu, Z. Li, B. Li, W. Liu, S. Zhang, K. Qiu, W. Zhu, Relationship between ferroptosis and mitophagy in cardiac ischemia reperfusion injury: A mini-review, PeerJ. 11 (2023) e14952. doi.org/10.7717/peerj.14952.

[17] S.J. Dixon, K.M. Lemberg, M.R. Lamprecht, R. Skouta, E.M. Zaitsev, C.E. Gleason, D.N. Patel, A.J. Bauer, A.M. Cantley, W.S. Yang, B. Morrison, B.R. Stockwell, Ferroptosis: An iron-dependent form of nonapoptotic cell death, Cell. 149 (2012) 1060–1072. doi.org/10.1016/j.cell.2012.03.042.

[18] W. Li, G. Feng, J.M. Gauthier, I. Lokshina, R. Higashikubo, S. Evans, X. Liu, A. Hassan, S. Tanaka, M. Cicka, H.M. Hsiao, D. Ruiz-Perez, A. Bredemeyer, R.W. Gross, D.L. Mann, Y.Y. Tyurina, A.E. Gelman, V.E. Kagan, A. Linkermann, K.J. Lavine, D. Kreisel, Ferroptotic cell death and TLR4/Trif signaling initiate neutrophil recruitment after heart transplantation, J. Clin. Invest. 129 (2019) 2293–2304. doi.org/10.1172/JCI126428.

[19] G. Miotto, M. Rossetto, M.L. Di Paolo, L. Orian, R. Venerando, A. Roveri, A.M. Vučković, V. Bosello Travain, M. Zaccarin, L. Zennaro, M. Maiorino, S. Toppo, F. Ursini, G. Cozza, Insight into the mechanism of ferroptosis inhibition by ferrostatin-1, Redox Biol. 28 (2020) 101328. doi.org/10.1016/j.redox.2019.101328.

[20] X. Fang, H. Wang, D. Han, E. Xie, X. Yang, J. Wei, S. Gu, F. Gao, N. Zhu, X. Yin, Q. Cheng, P.

Zhang, W. Dai, J. Chen, F. Yang, H.T. Yang, A. Linkermann, W. Gu, J. Min, F. Wang, Ferroptosis as a target for protection against cardiomyopathy, Proc. Natl Acad. Sci. U. S. A. 116 (2019) 2672–2680. doi.org/10.1073/pnas.1821022116.

[21] Q.M. Chen, Nrf2 for protection against oxidant generation and mitochondrial damage in cardiac injury, Free Radic. Biol. Med. 179 (2022) 133–143. doi.org/10.1016/j.freeradbiomed.2021.12.001.

[22] J. Wang, L. Lu, S. Chen, J. Xie, S. Lu, Y. Zhou, H. Jiang, Up-regulation of PERK/Nrf2/HO-1 axis protects myocardial tissues of mice from damage triggered by ischemia-reperfusion through ameliorating endoplasmic reticulum stress, Cardiovasc. Diagn. Ther. 10 (2020) 500–511. doi.org/10.21037/cdt-20-126.

[23] Q. Zhang, L. Wang, S. Wang, H. Cheng, L. Xu, G. Pei, Y. Wang, C. Fu, Y. Jiang, C. He, Q. Wei, Signaling pathways and targeted therapy for myocardial infarction, Sig. Transduct. Target. Ther. 7 (2022) 78. doi.org/10.1038/s41392-022-00925-z.

[24] Y. Zhang, P. Ye, H. Zhu, L. Gu, Y. Li, S. Feng, Z. Zeng, Q. Chen, B. Zhou, X. Xiong, Neutral polysaccharide from *Gastrodia elata* alleviates cerebral ischemia–reperfusion injury by inhibiting ferroptosis-mediated neuroinflammation via the NRF2 / HO −1 signaling pathway, CNS Neurosci. Ther. 30 (2024) e14456. doi.org/10.1111/cns.14456.

[25] C.X. Liu, X.Y. Guo, Y.B. Zhou, H. Wang, Therapeutic role of Chinese medicine targeting Nrf2/HO-1 signaling pathway in myocardial ischemia/reperfusion injury, Chin. J. Integr. Med. 30 (2024) 949–960. doi.org/10.1007/s11655-024-3657-0.

[26] Q. Long, T. Li, Q. Zhu, L. He, B. Zhao, SuanZaoRen decoction alleviates neuronal loss, synaptic damage and ferroptosis of AD via activating DJ-1/Nrf2 signaling pathway, J. Ethnopharmacol. 323 (2024) 117679. doi.org/10.1016/j.jep.2023.117679.

[27] T. Wang, Z. Jian, A. Baskys, J. Yang, J. Li, H. Guo, Y. Hei, P. Xian, Z. He, Z. Li, N. Li, Q. Long,

MSC-derived exosomes protect against oxidative stress-induced skin injury via adaptive regulation of the NRF2 defense system, Biomaterials. 257 (2020) 120264. doi.org/10.1016/j.biomaterials.2020.120264.

[28] S. Jiang, H. Li, L. Zhang, W. Mu, Y. Zhang, T. Chen, J. Wu, H. Tang, S. Zheng, Y. Liu, Y. Wu, X. Luo, Y. Xie, J. Ren, Generic Diagramming Platform (GDP): A comprehensive database of high-quality biomedical graphics, Nucleic Acids Res. 53 (2025) D1670–D1676. doi.org/10.1093/nar/gkae973.

[29] E.D. Muse, E.R. Kramer, H. Wang, P. Barrett, F. Parviz, M.A. Novotny, R.S. Lasken, T.A. Jatkoe, G. Oliveira, H. Peng, J. Lu, M.C. Connelly, K. Schilling, C. Rao, A. Torkamani, E.J. Topol, A whole blood molecular signature for acute myocardial infarction, Sci. Rep. 7 (2017) 12268. doi.org/10.1038/s41598-017-12166-0.

[30] Q. Wan, J. Tang, Y. Han, D. Wang, Co-expression modules construction by WGCNA and identify potential prognostic markers of uveal melanoma, Exp. Eye Res. 166 (2018) 13–20. doi.org/10.1016/j.exer.2017.10.007.

[31] P. Langfelder, S. Horvath, WGCNA: An R package for weighted correlation network analysis, BMC Bioinformatics. 9 (2008) 559. doi.org/10.1186/1471-2105-9-559.

[32] C. Liu, J. Liu, Y. Zhang, X. Wang, Y. Guan, Immune-related potential biomarkers and therapeutic targets in coronary artery disease, Front. Cardiovasc. Med. 9 (2022) 1055422. doi.org/10.3389/fcvm.2022.1055422.

[33] G. Song, Y. Zhang, X. Wang, C. Wei, Y. Qi, Y. Liu, L. Sun, An inflammatory prognostic scoring system to predict the risk for adults with acute coronary syndrome undergoing percutaneous coronary intervention, BMC Cardiovasc. Disord. 24 (2024) 728. doi.org/10.1186/s12872-024-04417-6.

[34] A. Schipper, M. Rutten, A. Van Gammeren, C.L. Harteveld, E. Urrechaga, F. Weerkamp, G. den Besten, J. Krabbe, J. Slomp, L. Schoonen, M. Broeren, M. van Wijnen, M.J.A.J. Huijskens, T. Koopmann,

B. van Ginneken, R. Kusters, S. Kurstjens, Machine learning-based prediction of hemoglobinopathies using complete blood count data, Clin. Chem. 70 (2024) 1064–1075. doi.org/10.1093/clinchem/hvae081.

[35] F. Jia, B. Zhang, W. Yu, Z. Chen, W. Xu, W. Zhao, Z. Wang, Exploring the cuproptosis-related molecular clusters in the peripheral blood of patients with amyotrophic lateral sclerosis, Comput. Biol. Med. 168 (2024) 107776. doi.org/10.1016/j.compbiomed.2023.107776.

[36] A. Kumari, M. Akhtar, R. Shah, M. Tanveer, Support matrix machine: A review, Neural Netw. 181 (2025) 106767. doi.org/10.1016/j.neunet.2024.106767.

[37] J. Hu, S. Szymczak, A review on longitudinal data analysis with random forest, Brief. Bioinform. 24 (2023) bbad002. doi.org/10.1093/bib/bbad002.

[38] A. Zhao, W. Lei, J. Tian, X. Wu, M. Li, Y. Zhang, X. Wu, X. Xu, J. Tang, Y. Yang, Z. Jin, Mangiferin attenuates myocardial ischemia reperfusion injury by regulating the GAS6 /Axl signaling pathway, Phytother. Res.. Published online January 9, 2025:ptr.8423. 39 (2025) 1388–1402. doi.org/10.1002/ptr.8423.

[39] Q. Yu, N. Zhang, X. Gan, L. Chen, R. Wang, R. Liang, J. Jian, EGCG attenuated acute myocardial infarction by inhibiting ferroptosis via miR-450b-5p/ACSL4 axis, Phytomedicine. 119 (2023) 154999. doi.org/10.1016/j.phymed.2023.154999.

[40] H. Tripathi, A. Al-Darraji, M. Abo-Aly, H. Peng, E. Shokri, L. Chelvarajan, R. R Donahue, B.M. Levitan, E. Gao, G. Hernandez, A.J. Morris, S.S. Smyth, A. Abdel-Latif, Autotaxin inhibition reduces cardiac inflammation and mitigates adverse cardiac remodeling after myocardial infarction, J. Mol. Cell. Cardiol. 149 (2020) 95–114. doi.org/10.1016/j.yjmcc.2020.09.011.

[41] A. Al-Darraji, D. Haydar, L. Chelvarajan, H. Tripathi, B. Levitan, E. Gao, V.J. Venditto, J.C. Gensel, D.J. Feola, A. Abdel-Latif, Azithromycin therapy reduces cardiac inflammation and mitigates adverse

cardiac remodeling after myocardial infarction: Potential therapeutic targets in ischemic heart disease, PLOS One Y. Guo (Ed.). 13 (2018) e0200474. doi.org/10.1371/journal.pone.0200474.

[42] A. Akhmedov, F. Montecucco, V. Braunersreuther, G.G. Camici, P. Jakob, M.F. Reiner, M. Glanzmann, F. Burger, F. Paneni, K. Galan, G. Pelli, N. Vuilleumier, A. Belin, J.P. Vallée, F. Mach, T.F. Lüscher, Genetic deletion of the adaptor protein p66Shc increases susceptibility to short-term ischaemic myocardial injury via intracellular salvage pathways, Eur. Heart J. 36 (2015) 516–26a. doi.org/10.1093/eurheartj/ehu400.

[43] X. Wu, J. Li, S. Chai, C. Li, S. Lu, S. Bao, S. Yu, H. Guo, J. He, Y. Peng, H. Sun, L. Wang, Integrated analysis and validation of ferroptosis-related genes and immune infiltration in acute myocardial infarction, BMC Cardiovasc. Disord. 24 (2024) 123. doi.org/10.1186/s12872-023-03622-z.

[44] Q. Zhou, R. Shi, J. Liu, Z. Liu, Identification and characterization of novel ferroptosis-related genes in acute myocardial infarction, Hum. Genomics. 18 (2024) 123. doi.org/10.1186/s40246-024-00693-7.

[45] J. Wu, H. Cai, Z. Lei, C. Li, Y. Hu, T. Zhang, H. Zhu, Y. Lu, J. Cao, X. Hu, Expression pattern and diagnostic value of ferroptosis-related genes in acute myocardial infarction, Front. Cardiovasc. Med. 9 (2022) 993592. doi.org/10.3389/fcvm.2022.993592.

[46] J. Quan, A.M. Bode, X. Luo, ACSL family: The regulatory mechanisms and therapeutic implications in cancer, Eur. J. Pharmacol. 909 (2021) 174397. doi.org/10.1016/j.ejphar.2021.174397.

[47] F. Al-Rashed, D. Haddad, A. Al Madhoun, S. Sindhu, T. Jacob, S. Kochumon, L.M. Obeid, F. Al-Mulla, Y.A. Hannun, R. Ahmad, ACSL1 is a key regulator of inflammatory and macrophage foaming induced by short-term palmitate exposure or acute high-fat feeding, iScience. 26 (2023) 107145. doi.org/10.1016/j.isci.2023.107145.

[48] H.A. Parkes, E. Preston, D. Wilks, M. Ballesteros, L. Carpenter, L. Wood, E.W. Kraegen, S.M. Furler,

G.J. Cooney, Overexpression of acyl-CoA synthetase-1 increases lipid deposition in hepatic (HepG2) cells and rodent liver in vivo, Am. J. Physiol. Endocrinol. Metab. 291 (2006) E737–E744. doi.org/10.1152/ajpendo.00112.2006.

[49] Q. Zhang, N. Li, L. Deng, X. Jiang, Y. Zhang, L.T.O. Lee, H. Zhang, ACSL1-induced ferroptosis and platinum resistance in ovarian cancer by increasing FSP1 N-myristylation and stability, Cell Death Discov. 9 (2023) 83. doi.org/10.1038/s41420-023-01385-2.

[50] J. Hong, X. Li, Y. Hao, H. Xu, L. Yu, Z. Meng, J. Zhang, M. Zhu, The PRMT6/STAT1/ACSL1 axis promotes ferroptosis in diabetic nephropathy, Cell Death Differ. 31 (2024) 1561–1575. doi.org/10.1038/s41418-024-01357-8.

[51] T. Li, X. Li, H. Meng, L. Chen, F. Meng, ACSL1 affects Triglyceride Levels through the PPARγ Pathway, Int. J. Med. Sci. 17 (2020) 720–727. doi.org/10.7150/ijms.42248.

[52] J. Wu, J. Luo, H. Cai, H. Zhu, Z. Lei, Y. Lu, X. Gao, L. Ni, Z. Lu, X. Hu, Expression characteristics of lipid metabolism-related genes and correlative immune infiltration landscape in acute myocardial infarction, Sci. Rep. 14 (2024) 14095. doi.org/10.1038/s41598-024-65022-3.

[53] C. Zhang, Z. Lv, H. Liang, F. Hu, H. Bi, Bioinformatics insights into ACSL1 and ACSL5: Prognostic and immune roles in low-grade glioma, BMC Cancer. 25 (2025) 226. doi.org/10.1186/s12885-025-13651-w.

[54] J.P. Friedmann Angeli, M. Schneider, B. Proneth, Y.Y. Tyurina, V.A. Tyurin, V.J. Hammond, N. Herbach, M. Aichler, A. Walch, E. Eggenhofer, D. Basavarajappa, O. Rådmark, S. Kobayashi, T. Seibt, H. Beck, F. Neff, I. Esposito, R. Wanke, H. Förster, O. Yefremova, M. Heinrichmeyer, G.W. Bornkamm, E.K. Geissler, S.B. Thomas, B.R. Stockwell, V.B. O'Donnell, V.E. Kagan, J.A. Schick, M. Conrad, Inactivation of the ferroptosis regulator Gpx4 triggers acute renal failure in mice, Nat. Cell Biol. 16 (2014)

1180–1191. doi.org/10.1038/ncb3064.

[55] J. Dupuy, E. Fouché, C. Noirot, P. Martin, C. Buisson, F. Guéraud, F. Pierre, C. Héliès-Toussaint, A dual model of normal vs isogenic Nrf2-depleted murine epithelial cells to explore oxidative stress involvement, Sci. Rep. 14 (2024) 10905. doi.org/10.1038/s41598-024-60938-2.

[56] L. Zhang, J. Zhang, Y. Jin, G. Yao, H. Zhao, P. Qiao, S. Wu, Nrf2 is a potential modulator for orchestrating iron homeostasis and redox balance in cancer cells, Front. Cell Dev. Biol. 9 (2021) 728172. doi.org/10.3389/fcell.2021.728172.

Table 1. Detailed information of the datasets

Dataset	Platform	AMI samples	Normal samples	Resource
GSE66360	GPL570	49	50	Homo sapiens
GSE20681	GPL4133	99	99	Homo sapiens
GSE214611	GPL24247	2	2	Mus musculus

Abbreviations: AMI, acute myocardial infarction

Table 2. List of primers used in the study

Gene	Sequence
ACSL1	Forward: TGGGGTGGAAATCATCAGCC
	Reverse: CATTGCTCCTTTGGGGTTGC
HO-1	Forward: AAGCCGAGAATGCTGAGTTCA
	Reverse: GCCGTGTAGATATGGTACAAGGA
NRF2	Forward: TCTTGGAGTAAGTCGAGAAGTGT
	Reverse: GTTGAAACTGAGCGAAAAAGGC
SLC7A11	Forward: GGCACCGTCATCGGATCAG
	Reverse: CTCCACAGGCAGACCAGAAAA
SLC40A1	Forward: ACCAAGGCAAGAGATCAAACC
	Reverse: AGACACTGCAAAGTGCCACAT
GAPDH	Forward: AGGTCGGTGTGAACGGATTTG
	Reverse: TGTAGACCATGTAGTTGAGGTCA

Table 3 Comparison of cardiac ultrasound between the AMI and Sham groups

Variables	AMI group	Sham group	p-value
IVS;d	0.78 (0.70, 0.85)	0.71 (0.64, 0.72)	0.008
IVS;s	1.15 ± 0.18	1.15 ± 0.15	0.902
LVID;d	4.69 ± 0.67	3.50 ± 0.38	<0.001
LVID;s	3.70 (3.37, 4.05)	2.13 (1.80, 2.42)	<0.001
LVPW;d	0.70 ± 0.12	0.75 ± 0.13	0.219
LVPW;s	0.92 ± 0.21	1.25 ± 0.16	<0.001
EF (%)	39 (31, 44)	71 (66, 74)	<0.001
FS	19 (14, 21)	39 (36, 42)	<0.001
LV Mass	128 (116, 151)	76 (67, 94)	<0.001
LV Mass (Corrected)	103 (93, 121)	61 (54, 75)	<0.001
LV Vol;d	96 (81, 110)	51 (41, 61)	<0.001
LV Vol;s	58 (47, 72)	15 (10, 21)	<0.001

Abbreviations: AMI, acute myocardial infarction; IVS d, interventricular septal end diastole; IVS s, interventricular septal end systole; LVID d, left ventricular internal diameter end diastole; LVID s, left ventricular internal diameter end systole; LVPW d, left ventricular posterior wall end diastole; LVPW s, left ventricular posterior wall end systole; EF, ejection fraction; FS, fractional shortening; LV, left ventricular

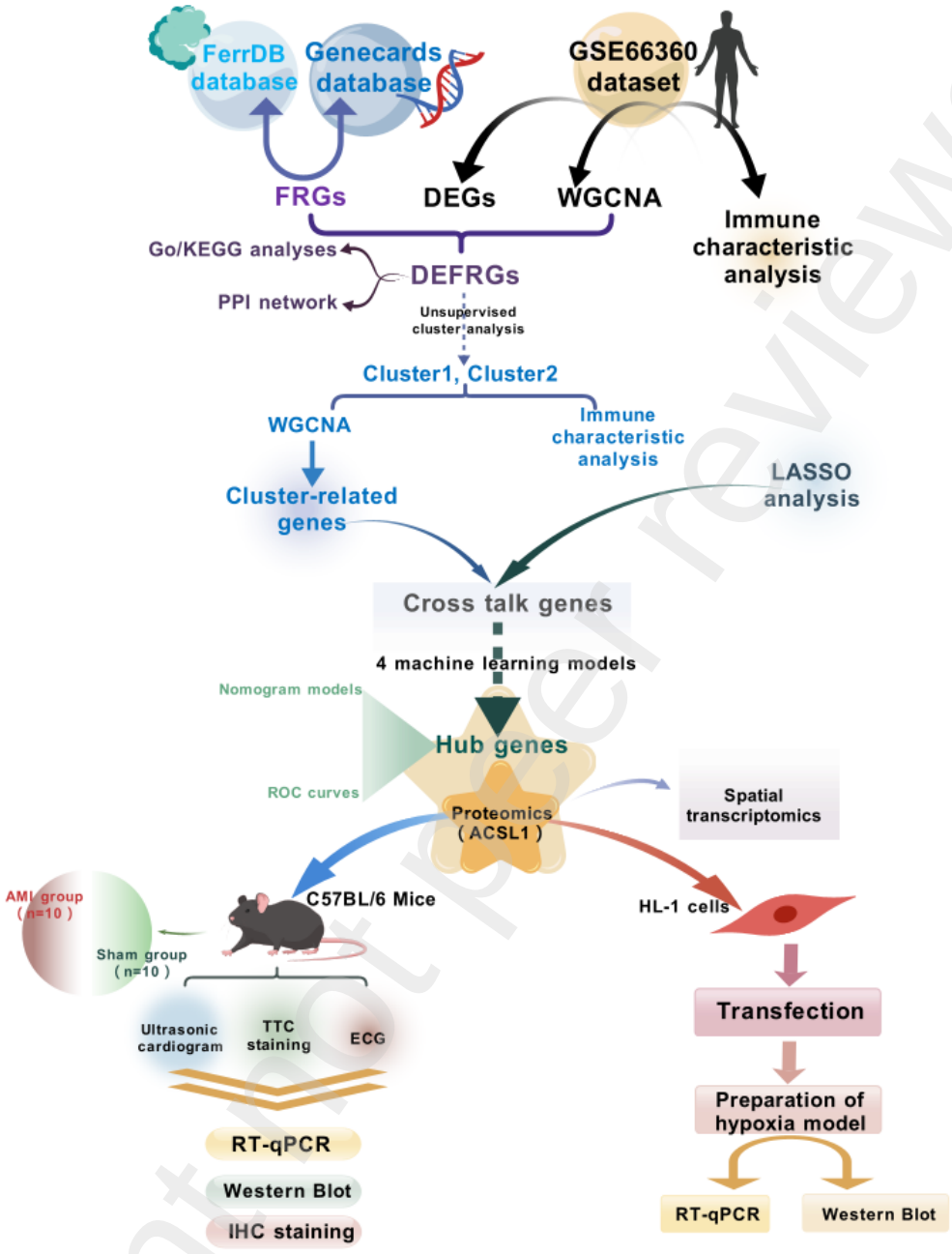

Fig. 1. The basic framework of this study

Abbreviations: FRGs, ferroptosis-related genes; DEGs, differentially expressed genes; WGCNA, weighted gene co-expression network analysis; DEFRGs, differentially expressed ferroptosis-related genes; LASSO, least Absolute Shrinkage and Selection Operator; KEGG, Kyoto Encyclopedia of Genes and Genomes; GO, Gene Ontology; PPI, protein-protein interaction; ELISA,

enzyme-linked immunosorbent assay; RT-qPCR, Real-Time quantitative PCR; ROC, receiver operating characteristic curve; IHC, Immunohistochemical staining.

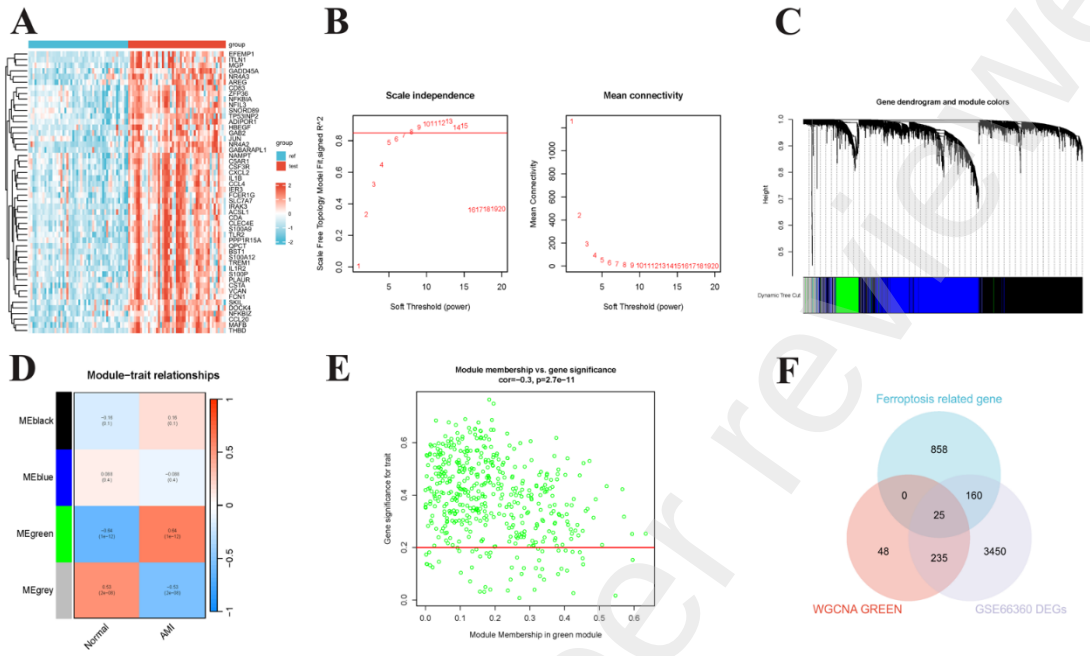

Fig. 2. Construction of the co-expression network for differentially expressed genes in AMI

(A) Heatmap of the expression patterns of DEGs between AMI and normal controls in GSE66360. (B) Network topology analysis for the soft thresholding powers. (C) Dendrogram of clustered genes with topologically overlapping based variability and specified module colors. (D) Module trait correlations. Each column matches a trait, and each row matches a module eigengene. Each unit cell includes the corresponding p-value and correlation. (E) A scatterplot of Module Membership (MM) in the green module vs. Gene Significance (GS) for AMI. (F) The Venn diagram of ferroptosis-related genes, WGCNA GREEN, and GSE66360 DEGs. Abbreviations: AMI, Acute myocardial infarction; DEGs, differentially expressed genes.

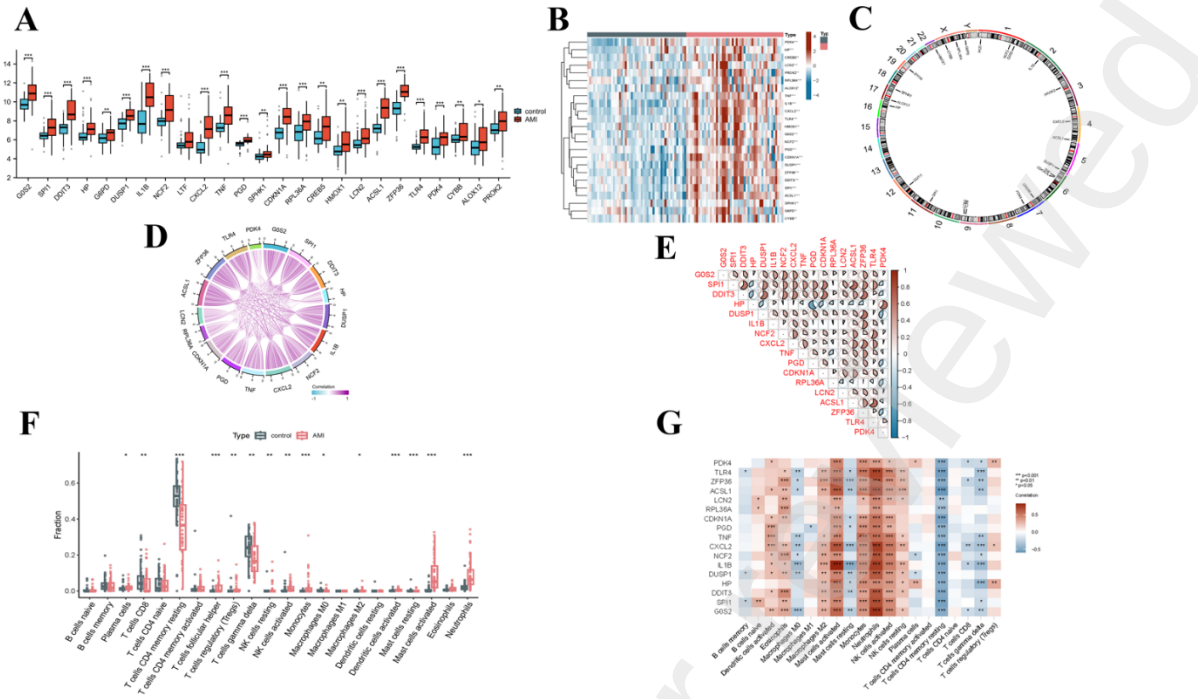

Fig. 3. Identification of immune characteristics and DEFRGs in AMI

(A) Box diagram of the expression profiles of 25 FRGs. (B) Heatmap of the expression patterns of 24 DEFRGs between AMI and normal controls. (C) Location of the 24 DEFRGs on the chromosome. (D) Gene relationship circle diagram for the 17 DEFRGs. The purple and blue lines represent positive and negative correlations, respectively. (E) The relationship between DEFRGs. The correlation coefficients were labeled by the area of the pie chart. (F) Box diagram of the fractions of 22 immune infiltrating cells using the CIBERSORT algorithm. (G)The relationship between 17 DEFRGs and 20 immune infiltrating cells. Significance levels were indicated by *p < 0.05, **p < 0.01, ***p < 0.001. Abbreviations: AMI, Acute myocardial infarction; DEFRGs, differentially expressed ferroptosis-related genes.

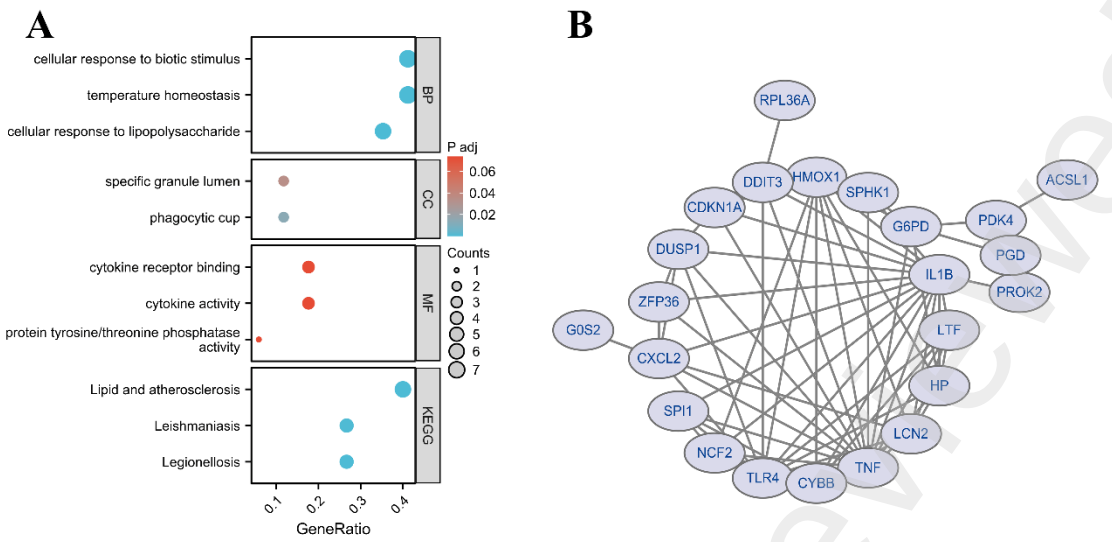

Fig. 4. Functional analysis of DEFRGs and the protein-protein interaction (PPI) network

(A) Bubble plots of GO and KEGG pathway enrichment analysis results. (B) 23 critical DEFRGs based on the STRING database filtered into the PPI network. Abbreviations: DEFRGs, differentially expressed ferroptosis-related genes; GO, gene ontology; KEGG, Kyoto Encyclopedia of Genes and Genomes.

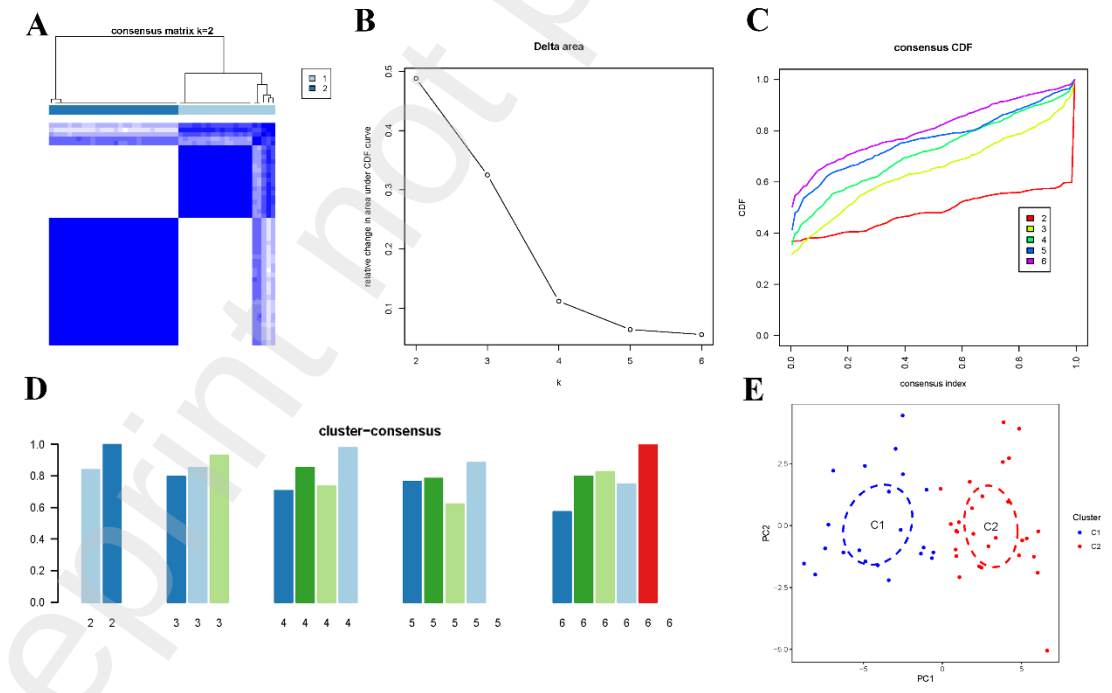

Fig. 5. Consensus clustering based on DEFRGs expression matrices

(A) Consensus clustering matrix at k = 2. (B) Relative change in area under CDF delta curves. (C)

Cumulative distribution function (CDF) consensus clustering at k = 2–6. (D) Consensus clustering score. (E) PCA plot of the two clusters. The points of the scatterplot denote each sample of the two main components of the cluster (PC1 and PC2) based on the DEFRGs expression profiles. Abbreviations: DEFRGs, differentially expressed ferroptosis-related genes; PCA, Principal component analysis.

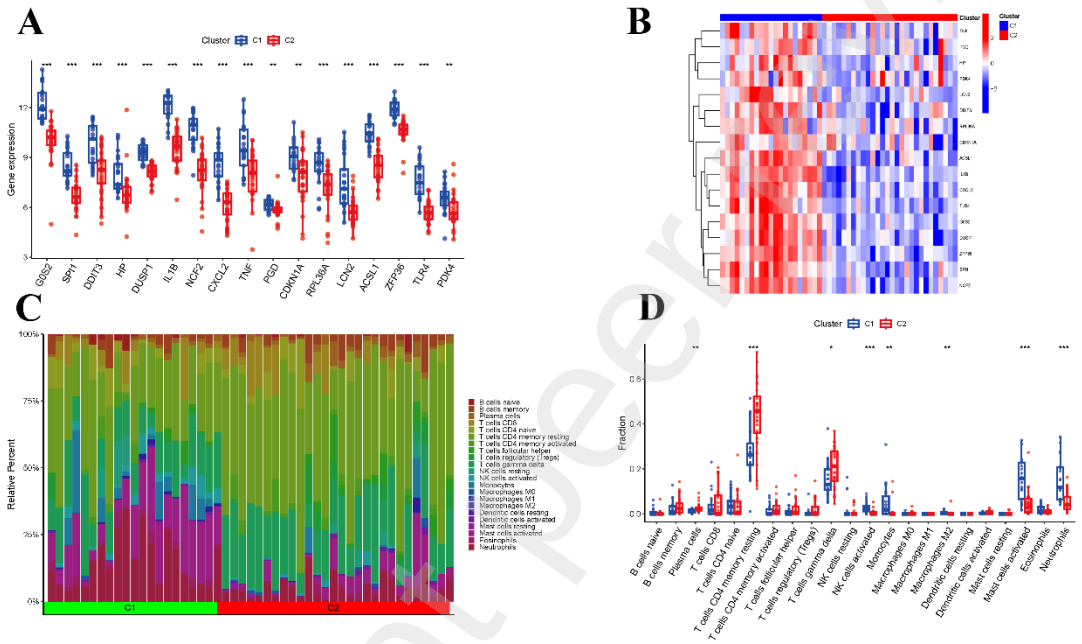

Fig. 6. Gene abundances, immune characteristics, and biological processes of different ferroptosis-related clusters

(A) and (B) presented the expression patterns of 17 DEFRGs in two distinct ferroptosis-related phenotypes in terms of boxplot and heatmap. (C) The relative abundance of 22 infiltrating immune cells between the two phenotypes. (D) Boxplot of the ratio of 22 species of immune-infiltrated cells with the CIBERSORT algorithm. Abbreviations: DEFRGs, differentially expressed ferroptosis-related genes.

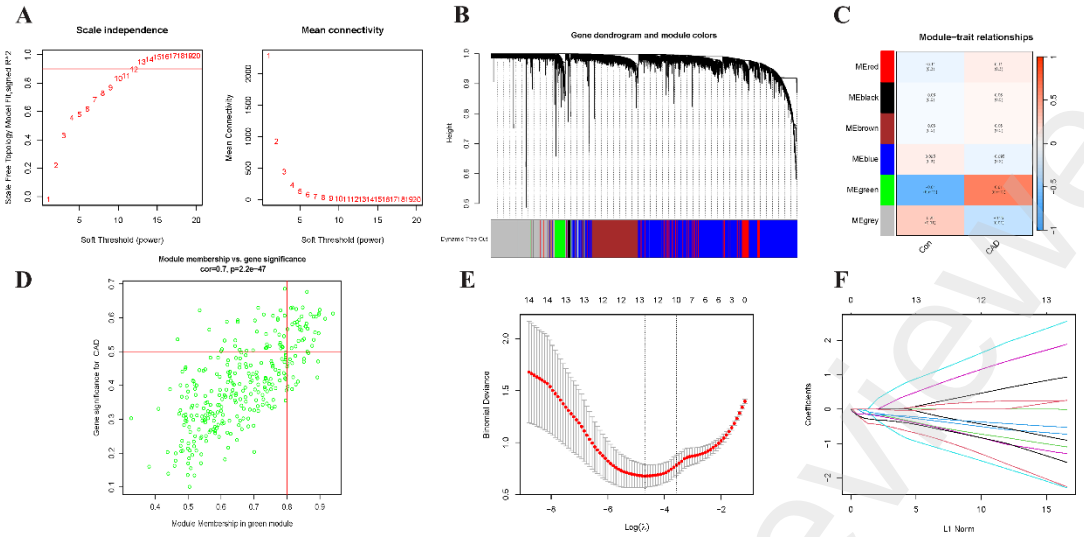

Fig. 7. Identification of the critical gene modules related to the ferroptosis phenotypes

(A) Gene clustering dendrogram based on topological overlap and specified module colors. (B) Heatmap plot of the associations between six modules. (C) The correlation between clinical status and module eigengenes. Each column matches a trait, and each row corresponds to a module eigengene. Each unit cell includes the corresponding p-value and correlation. (D) Scatterplot of Module Membership (MM) vs. Gene Significance (GS) in the green module. (E) Ten-fold cross-validation for tuning parameter selection in the LASSO model. (F) LASSO coefficient profiles of the DEFRGs. Abbreviations: DEFRGs, differentially expressed ferroptosis-related genes.

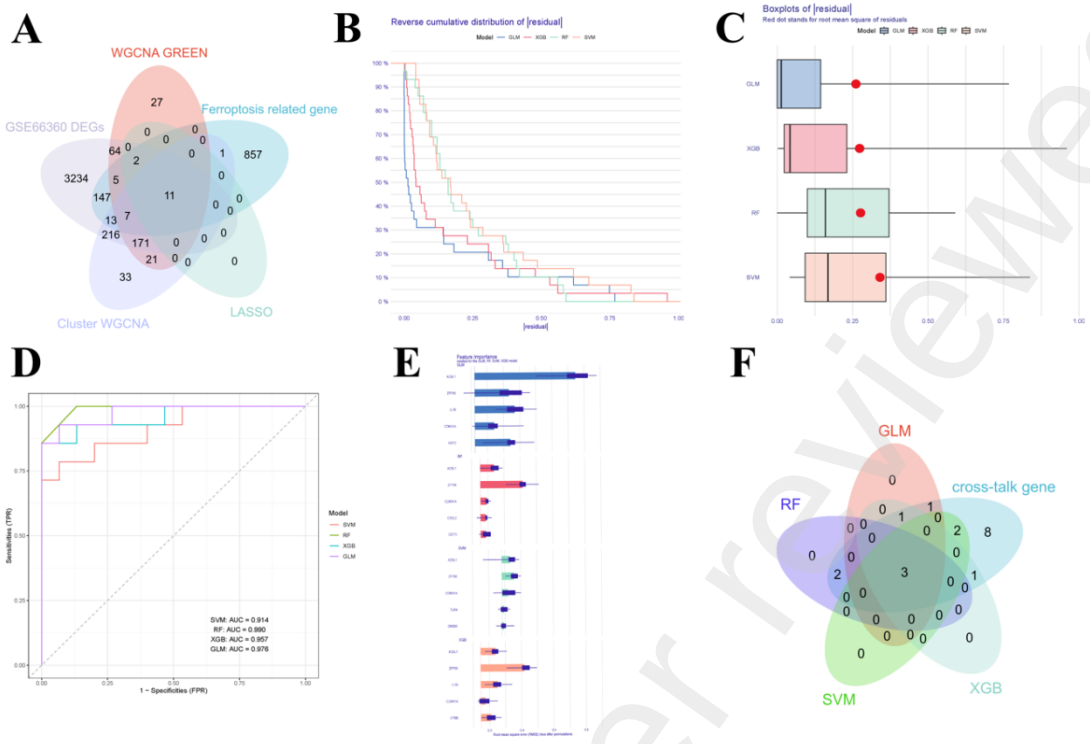

Fig. 8. Selection of the optimal machine learning model

(A) The cross-sections between module-associated genes of ferroptosis phenotypes and module-associated genes in AMI. (B) Reverse cumulative distributions of the four modes. (C) The residuals of four models were shown in the boxplot. (D) ROC curves analysis of the RF, SVM, XGB, and GLM models. (E) The essential characteristics of the machine learning models. (F) The Venn diagram of the crosstalk gene and four machine learning models. Abbreviations: AMI, Acute myocardial infarction; ROC, receiver operating characteristic; XGB, extreme Gradient Boosting; GLM, the generalized linear model; the RF, random forest model; SVM, support vector machine model.

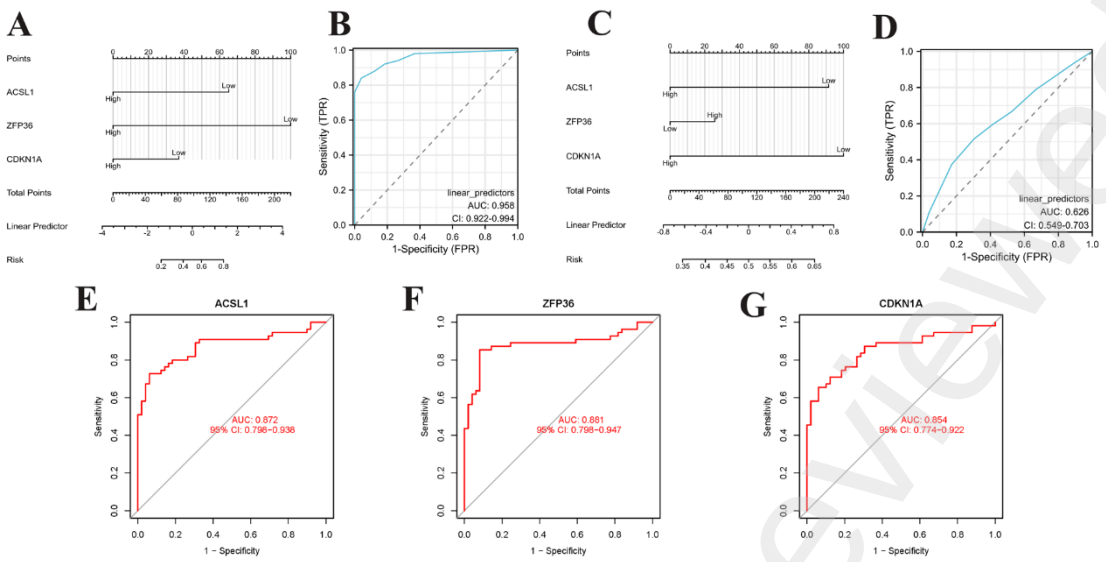

Fig. 9. Construction and validation of a prediction nomogram

(A) A nomogram model with three feature genes in the GSE66360 dataset. (B) The ROC curve for evaluating the diagnostic performance of the 3-gene signature model in the GSE66360 dataset. (C) Construction of a nomogram model with three feature genes in the GSE20681 dataset as an external validation. (D) ROC curve for validating the diagnostic model's performance in the GSE20681 dataset. (E) ROC curve analysis of one of the hub genes, ACSL1, in the GSE66360 dataset. (F) ROC curve analysis of ZFP36. (G) ROC curve analysis of CDKN1A. Abbreviations: ROC, receiver operating characteristic.

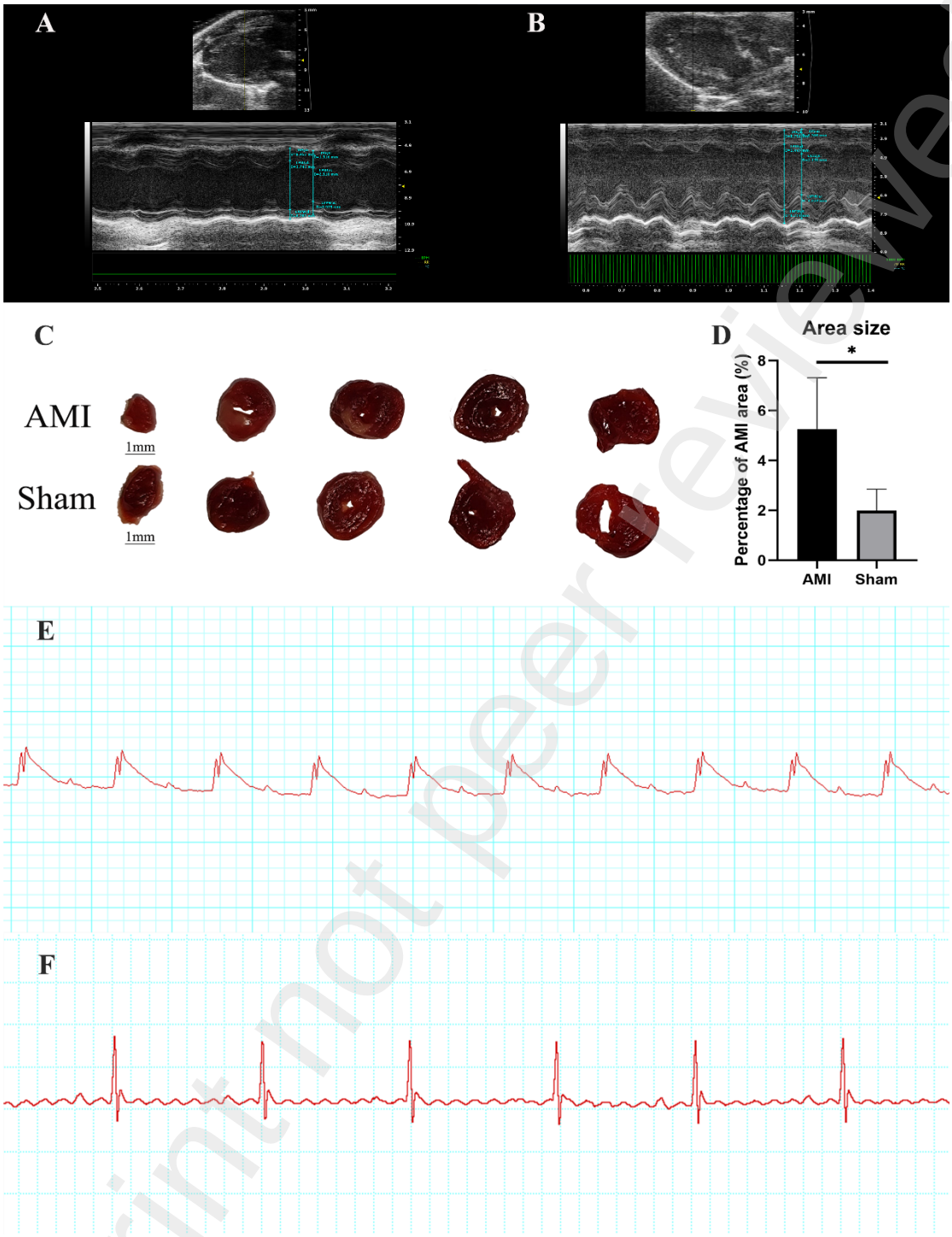

Fig. 10. Validation of AMI model

(A) Representative images of cardiac ultrasound results for the AMI group. (B) Representative images of cardiac ultrasound results for the Sham group. (C) (D) Representative images of TTC staining results for the AMI and Sham groups. (E) Representative images of electrocardiogram results for the AMI group. (F) Representative images of electrocardiogram results for the Sham

group. *p < 0.05. Abbreviations: AMI, Acute myocardial infarction.

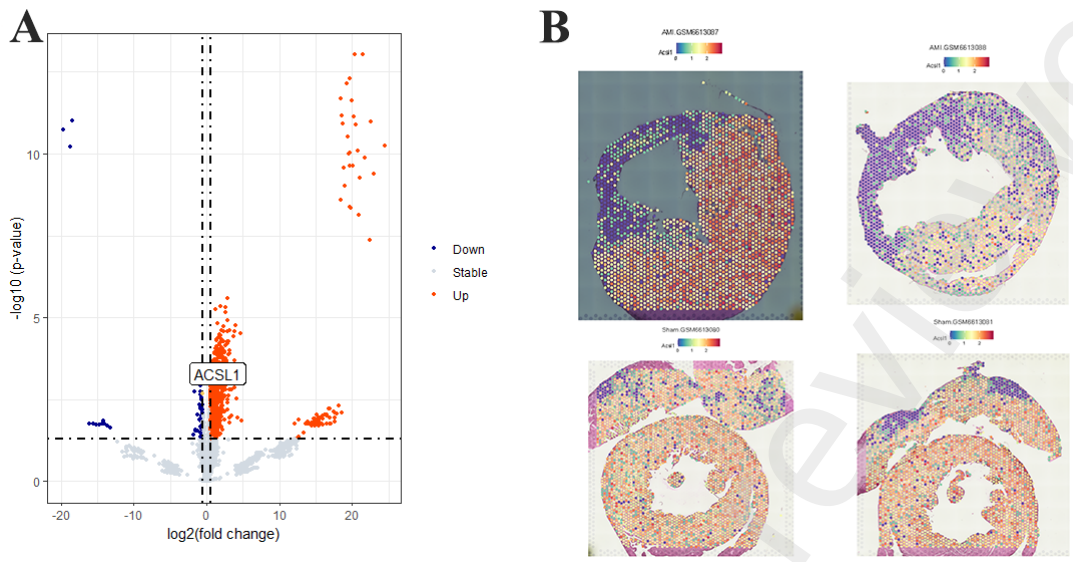

Fig.11. Identification of hub gene

(A) The label-free quantitative proteomic analysis. (B) Spatial transcriptomics analysis of ACSL1.

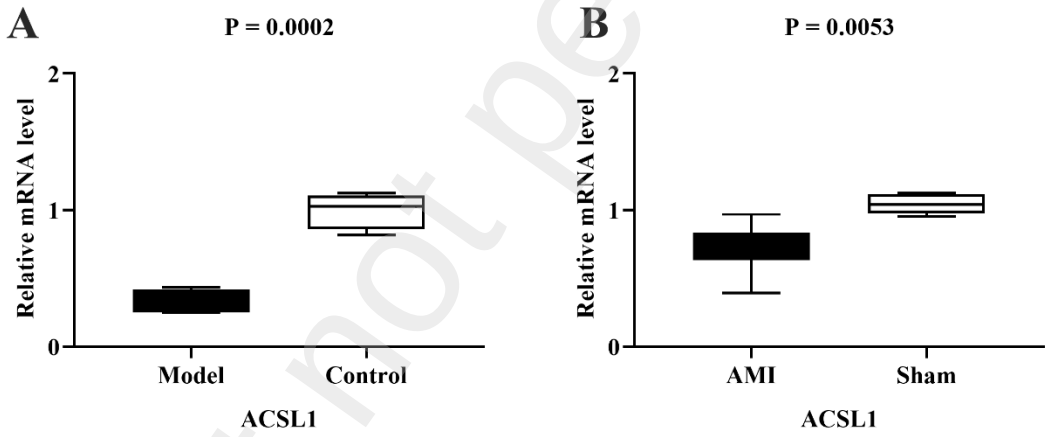

Fig. 12. Validation of hub gene in vivo and vitro by RT-qPCR

(A) ACSL1 expression in hypoxic model and control HL-1 cells was evaluated. (B) ACSL1 expression in AMI and sham mouse cardiac tissues was evaluated. Abbreviations: AMI, Acute myocardial infarction.

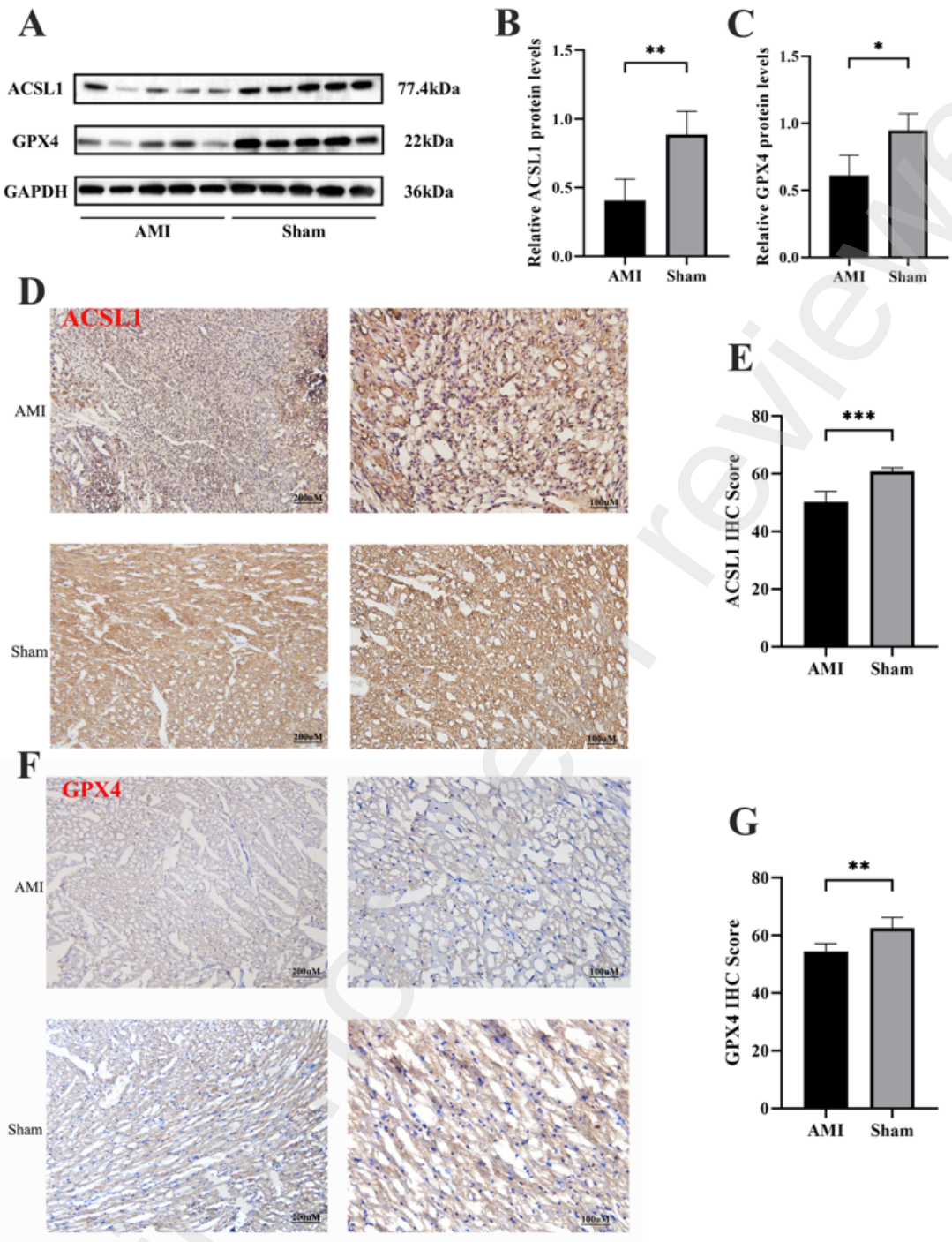

Fig. 13. The validation of ACSL1 at the protein level and the occurrence of ferroptosis

(A) The result of Western blot analysis. (B) Western blotting analysis of total ACSL1 in the AMI and sham mouse cardiac tissues, n = 10. (C) Western blotting analysis of total GPX4 in the AMI and sham mouse cardiac tissues, n = 10. (D) (E) Representative immunohistochemical images of ACSL1-positive cells in the AMI and sham mouse cardiac tissues, n = 10. (F) (G) Representative

immunohistochemical images of GPX4-positive cells in the AMI and sham mouse cardiac tissues, n = 10. *p < 0.05, **p < 0.01, ***p < 0.001, ****p < 0.0001. Abbreviations: AMI, Acute myocardial infarction.

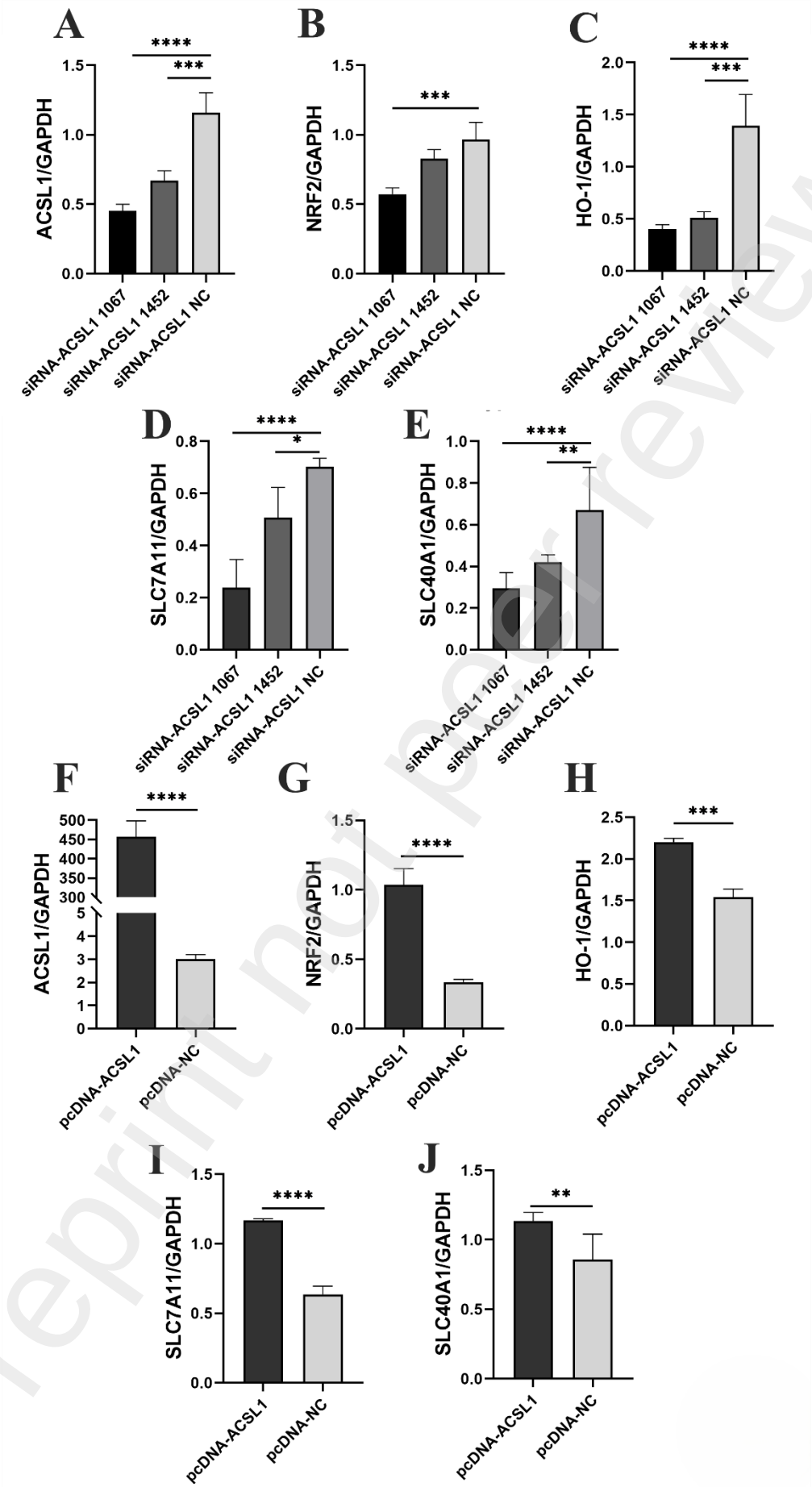

Fig. 14. The results of PCR of silence and overexpression of ACSL1 in HL-1 cells

(A) (B) (C) (D) (E) The expression levels of ACSL1, NRF2, HO-1, SLC7A11, and SLC40A1 in HL-1 cells with ACSL1 silencing in a hypoxic environment. (F) (G) (H) (I) (J) The expression levels of ACSL1, NRF2, HO-1, SLC7A11, and SLC40A1 in HL-1 cells with ACSL1 overexpression in a hypoxic environment. *$p < 0.05$, **$p < 0.01$, ***$p < 0.001$, ****$p < 0.0001$.

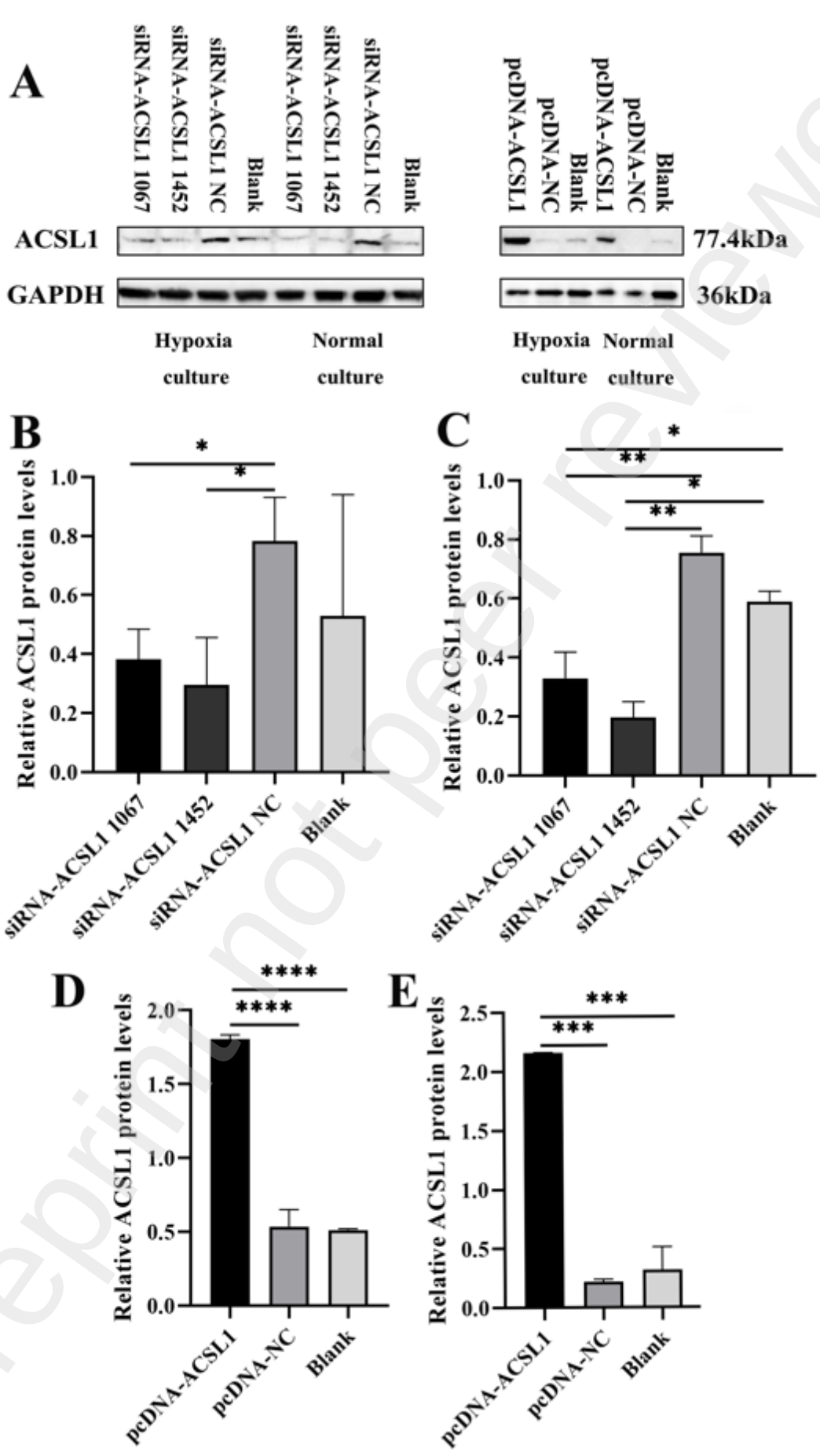

Fig. 15. The silencing and overexpression of ACSL1 in HL-1 cells at the protein level

(A) Western blot analysis of the silencing or overexpression of ACSL1. (B) The results of silencing the protein expression of ACSL1 in the hypoxic model. (C) The results of silencing the protein expression of ACSL1 in the control group. (D) The results of overexpressing the protein expression situation of ACSL1 in the hypoxic model. (E) The results of overexpressing the protein expression situation of ACSL1 in the control group. *$p < 0.05$, **$p < 0.01$, ***$p < 0.001$, ****$p < 0.0001$.